


RESEARCH ARTICLE

Open Access



Lithological structure of western Pacific lithosphere reconstructed from mantle xenoliths in a petit-spot volcano

Kazuto Mikuni^{1*} , Naoto Hirano^{1,2}, Norikatsu Akizawa³, Junji Yamamoto⁴, Shiki Machida⁵, Akihiro Tamura⁶, Yuuki Hagiwara^{7,8} and Tomoaki Morishita⁶

Abstract

The lithospheric mantle, formed at the mid-ocean ridge as a residue of crustal production, comprises theoretically depleted peridotite, but more fertile components (e.g., lherzolite and pyroxenite) have been reported, creating an enigmatic picture of the lithosphere. The oceanic lithosphere has also been found to be locally modified by intraplate magmatism as proposed from geochemistry of mantle xenolith. Petit-spot xenoliths are particularly notable as direct evidence of old lithospheric mantle and expected to retain essential information about oceanic lithosphere prior to its subduction. In this study, we report on the lithological structure of Pacific lithosphere aged at 160 Ma, just subducting into Mariana Trench, based on petrology and chemistry of ultramafic xenoliths from a petit-spot knoll, and then, we suggest the occurrence of petit-spot melt infiltration resulting in mantle metasomatism and formation of pyroxene-rich vein. Our petit-spot ultramafic xenoliths can be divided into three main types: a depleted peridotite as a residue of crust production, an enriched peridotite, and fertile pyroxenites as the product of melt–rock interactions prior to entrapment. Geothermobarometry also suggests that the depleted peridotite was derived from the uppermost lithospheric mantle, whereas the enriched peridotite and Al-augite pyroxenites were obtained from deeper layers of the lithosphere. Moreover, thermal gradient of the lithosphere estimated from these data is considerably hotter than pristine geotherm estimated on the basis of plate age. Hence, we could illustrate that the oldest portion of the Pacific lithosphere (160 Ma), which was not observed before, was locally fertilized and heated by prior multiple petit-spot magmatic events, and pyroxene-rich metasomatic veins penetrated from the base to the middle/upper lithosphere. Such local lithospheric fertilization is plausible at the plate-bending field, and the nature of Pacific Plate subducting into Mariana Trench may be partly different from what has been assumed so far.

Keywords: Petit-spot, Lithosphere, Pacific plate, Mantle xenolith, Metasomatism, Melt–rock interaction

1 Introduction

Pacific lithosphere, formed at the triple-ridge junction in Early Jurassic, is composed of the basaltic crust and lithospheric mantle (e.g., Müller et al. 2008; Boschman and Van Hinsbergen 2016). In theory, a high degree of melting is expected in the uppermost mantle column as a consequence of basaltic crust production in the mid-ocean ridge and upper lithospheric mantle supposedly comprises of depleted peridotite (e.g., Langmuir et al. 1992).

*Correspondence: kazuto.mikuni.t6@dc.tohoku.ac.jp

¹ Graduate School of Science, Tohoku University, 6-3 Aramaki-Aoba, Aoba-Ku, Sendai 980-8578, Japan

Full list of author information is available at the end of the article

Studies on the oceanic lithospheric mantle have been conducted in limited areas such as ophiolites (e.g., Meckel et al. 2003; Anma et al. 2009; Akizawa and Arai 2009; Dilek and Morishita 2009; Dilek and Furnes 2014; Goodenough et al. 2014), abyssal peridotites exposed along transform faults in mid-ocean ridges (e.g., Dick and Natland 1996; Niu et al. 1997; Mallick et al. 2015; Regelous et al. 2016; Warren 2016), oceanic core complexes at slow-spreading ridges (e.g., Ohara et al. 2001; Escartín et al. 2008; Blackman et al. 2009; Olive et al. 2010; Pressling et al. 2012; Akizawa et al. 2021; Sen et al. 2021; Harigane et al. 2022), and mantle xenoliths in intraplate volcanoes (e.g., Clague 1988; Hauri and Hart 1994; Sen et al. 2005; Bizimis et al. 2007, 2013; Jackson et al. 2016; Snortum et al. 2019). These studies revealed that the lithospheric mantle mainly comprises depleted peridotites, but a significant number of fertile components cross-cutting the depleted peridotites were also recognized. Although the compositional diversity can be caused by mid-ocean ridge magmatism as a function of multiple melt infiltrations or the vertical variations in degree of partial melting (Plank and Langmuir 1992; Akizawa et al. 2012; Rochat et al. 2017), local fertilizations can occur via intraplate volcanism (e.g., Hauri et al. 1993).

A number of studies on mantle xenoliths, brought by hotspot magmatism on Pacific Plate, have proved the occurrence of chemical, thermal, and petrological modification of lithospheric mantle by intrusive magma (Tracy 1980; Fodor et al. 1982; Clague 1988; Hauri and Hart 1994; Qi et al. 1994; Dieu 1995; Burnard et al. 1998; Sen et al. 2005; Bizimis et al. 2007, 2013; Jackson et al. 2016; Snortum et al. 2019). Such local magma infiltration in the lithosphere has also been suggested at the older Pacific Plate just subducting into a trench based on fresh mantle xenoliths brought by petit-spot magma (Yamamoto et al. 2009, 2014; Pilet et al. 2016).

Mantle xenoliths from petit-spot volcanoes can provide direct information of the Pacific lithosphere below an abyssal plain. Petit-spot magma is derived from the lithosphere–asthenosphere boundary, and its xenoliths certainly originate from the lithosphere (Hirano et al. 2006). For example, the geochemistry and geothermobarometry of petit-spot mantle xenoliths revealed that the old portion (130–135 Ma) of the Pacific lithosphere is thermally and/or compositionally modified by prior petit-spot magmatism events, and it has been suggested that the nature of the subducting lithosphere might be different from what we had previously assumed (Yamamoto et al. 2009, 2014; Pilet et al. 2016). Here, we report the various small ultramafic xenoliths derived from the oldest part of Pacific lithosphere (ca. 160 Ma) to discuss the existence of residual mantle and the occurrence of local metasomatism resulted from intrusive petit-spot magma.

2 Background

2.1 Petit-spot volcanic field in the western Pacific

Petit-spot is a form of small scale magmatism caused by lithospheric stresses arising from plate-subduction; it is believed to originate from the lithosphere–asthenosphere boundary (Hirano et al. 2006; Machida et al. 2015, 2017). The petit-spot volcanic cluster in this study, first reported by Yamamoto et al. (2018), is surrounded by Cretaceous seamounts and oceanic islands of the Western Pacific Seamount Province (WPSP; Koppers et al. 2003) (Fig. 1a). The study area is in the abyssal plain southeast of Minamitorishima (Marcus) Island, corresponding to the oldest portion of the Pacific Plate, at the northern tip of the Jurassic Quiet Zone (Fig. 1b) (Tivey et al. 2006). Young and fresh petit-spot lava samples were collected for the first time from a knoll in this cluster by two submersible diversions of 6K#1203 and 6K#1206 using a *SHINKAI 6500* deep-submergence vehicle (DSV) during the YK10-05 research cruise of the R/V Yokosuka from the Japan Agency for Marine-Earth Science and Technology (Fig. 1c). According to geochemical features and estimated eruption ages (< 3 Ma), this knoll is expected to have erupted owing to a swell in the plate that developed in response to subduction beneath the Mariana Trench (Hirano et al. 2019). Another petit-spot knoll was newly investigated by submersible diving of 6K#1466 during the YK16-01 research cruise (Figs. 1c, 2a). Notably, the basalt samples include ultramafic xenoliths, as stated later in the sample description and petrography section.

2.2 Xenoliths from Pacific lithosphere

A number of studies reported on mantle xenoliths in the Pacific Plate: Hawaiian Islands, Samoan Islands, Cook Islands, Tahiti, seamounts on the WPSP, and petit-spot volcanoes (e.g., Tracy 1980; Fodor et al. 1982; Clague 1988; Hauri and Hart 1994; Qi et al. 1994; Dieu 1995; Burnard et al. 1998; Sen et al. 2005; Hirano et al. 2006; Bizimis et al. 2007, 2013; Jackson et al. 2016; Snortum et al. 2019). Xenoliths from the Hawaiian Island chain are mainly harzburgite, lherzolite, wehrlite, dunite, and crustal rocks, principally from Kilauea lava, Honolulu Volcanics, and Loihi seamount (e.g., Jackson and Wright 1970; Clague 1988; Wagner and Grove 1998). In the Honolulu Volcanics, diverse types of xenoliths including harzburgite, lherzolite, pyroxenite (with and without garnet), and dunite have been reported mainly in rejuvenated-stage lava (Clague and Frey 1982; Roedder 1983; Clague 1988; Sen et al. 2005; Bizimis et al. 2005, 2007). The Samoan xenoliths are harzburgite and dunite, which show various degrees of light-rare-earth element (LREE) concentrations in correlation with equilibrium temperatures, implying that the carbonatite and/or silicate metasomatism was due to the early stage of the Samoan mantle

plume rather than to host magmatism (Hauri and Hart 1994; Burnard et al. 1998; Ashley et al. 2020; Byerly et al. 2021). Olivine nephelinite on Aitutaki of Cook Islands and basalts in Tahiti include ultramafic xenoliths of both Cr-diopside series and Al-augite series, suggesting previous melt infiltrations before entrapment as well (Tracy 1980; Fodor et al. 1982; Qi et al. 1994). Dieu (1995) classified ultramafic xenoliths from Limalok guyot and MIT guyot in the WPSP into type 1 (residual mantle) and type 2 (cumulate from basaltic melt), suggesting the occurrence of carbonatite metasomatism in the residual mantle. It is almost certain that several portions of the Pacific lithosphere below the hotspot seamounts/islands were modified by plume-related magmatism, although some depleted xenoliths were reported.

Xenoliths from petit-spot volcanoes are unique samples having information about the older part of Pacific lithosphere just before subduction. Xenoliths from previously reported petit-spots are basalt (crust origin), dolerite, gabbro, and peridotite (Hirano et al. 2006). Studies on ultramafic xenoliths and concomitant olivine xenocrysts in the petit-spot basalts have been limited to those in the NW Pacific (Hirano et al. 2004; Harigane et al. 2011; Yamamoto et al. 2009, 2014; Pilet et al. 2016). Peridotite xenoliths from the northwestern (NW) Pacific petit-spot showing a deep origin ($< \sim 45$ km: Yamamoto et al. 2014) have contributed to the understanding of deeper portions of the lithosphere. In contrast, the fact that no xenoliths originating from layers deeper than ~ 45 km have been reported has helped to clarify the petit-spot

magma eruption process (i.e., magma stagnation with fractionation in the middle of the lithosphere; Machida et al. 2017). Based on geochemical results and a numerical simulation, Pilet et al. (2016) suggested that the lithospheric mantle was locally refertilized with formation of metasomatic veins because of multiple petit-spot magmatism events before entrapment. This was supported by noble gas isotopic ratios and geothermobarometry of petit-spot mantle xenoliths (Yamamoto et al. 2009, 2014). Such magma percolation in the oceanic lithosphere could occur ubiquitously because petit-spot magmatism is plausibly a universal geological phenomenon at the plate-bending fields and/or where the small amount of volatiles exists below lithosphere (e.g., Hirano et al. 2008; Hirano 2011).

3 Sample description and petrography

Basalt samples were collected at near the summit of the small conical knoll located approximately 100 km south of Minamitorishima Island (Figs. 1c, 2a). The conical knoll is ca. 160 m in height and ca. 1 km in diameter, with a summit water depth of ca. 5300 m (Fig. 2a). The volume of the volcanic edifice is estimated at approximately 0.04 km^3 , which is comparable to those of other petit-spot knolls in the NW Pacific ($0.001\text{--}1 \text{ km}^3$; Hirano et al. 2008). The image of outcrop is shown in Machida et al. (2021) which explored the petit-spot lava flows by combining a sub-bottom profiler with a multi-beam echo sounder. Three basaltic lava samples, named 6K#1466R6-001, 6K#1466R7-001, and 6K#1466R7-003,

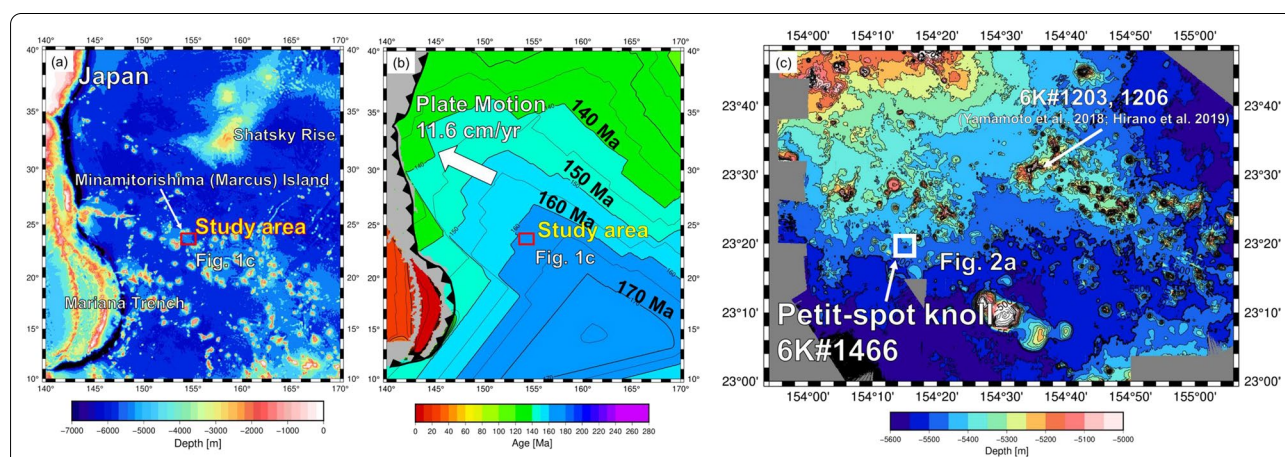
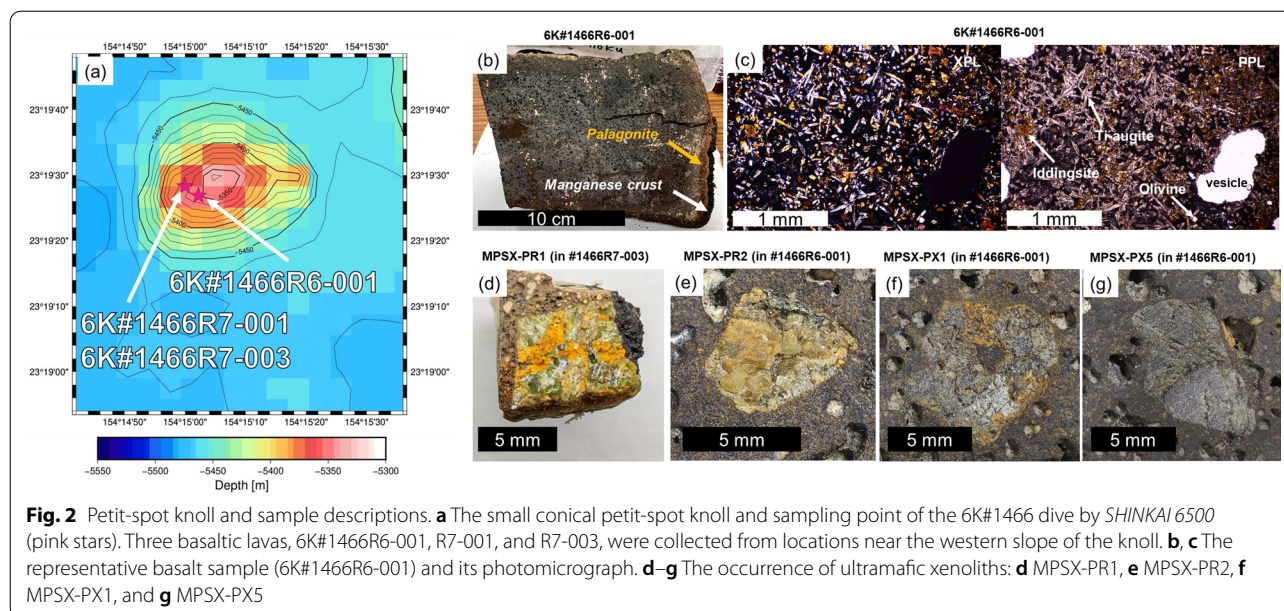


Fig. 1 Bathymetric and seafloor age map around the study area. **a** The bathymetry of the western Pacific near the Mariana Trench. The red box shows the study area, to the southeast of Minamitorishima (Marcus) Island. Bathymetric data are from ETOPO1 (NOAA National Geophysical Data Center; <http://www.ngdc.noaa.gov/>). **b** The seafloor age map of same area as in (a). This study area is within a 160–170 Ma region called the Jurassic Quiet Zone (JQZ) (Tivey et al. 2006). The absolute motion of the Pacific Plate in this area is from Gripp and Gordon (1990). The seafloor age data are from Müller et al. (2008). **c** A detailed bathymetric map of the study area. The onboard multibeam data are from the YK10-05 cruise by JAMSTEC. The petit-spot knoll explored in this study, surveyed by the 6K#1466 dive, is displayed in a white box; that surveyed by dives 6K#1203 and 6K#1206 was reported by Hirano et al. (2019)



contain small (<1 cm in diameter) xenoliths and xenocrysts. Seven xenoliths, one xenocryst, and some isolated (handpicked) clinopyroxene xenocrysts were selected from the three samples.

3.1 Host basalt

The three host basalts are highly vesicular (20–40 vol.% vesicularity) and mantled by 4.3–5.2-mm-thick manganese crusts over 5.5–6.6-mm-thick palagonite rinds (hydrated quench glass) (Fig. 2b). The basalts contain needle-shaped Ti-augite (50–400 μm in size), subhedral olivine with aureoles of iddingsite (up to 100 μm in size), opaque minerals (up to 10 μm in size), glass, and crystallite, without remarkable phenocrysts (Fig. 2c). Young eruption ages were estimated, ranging from 5.2 to 0.4 Ma using the average thickness of manganese crusts and their deposition rate at the seafloor (1–10 mm/Myr; Hein et al. 1999) or ranging from 2.2 to 0.2 Ma using the average thickness of palagonite and its hydration rate (0.03–0.3 mm/Myr; Moore et al. 1985). These are based on macroscopic and microscopic observations.

3.2 Xenoliths and xenocrysts

As the xenoliths are too small to determine lithology from the modal composition (<1 cm in diameter; Fig. 2d–g and Additional file 1: Fig. S1), we simply use the terms *peridotite* for olivine-rich xenoliths and *pyroxenite* for pyroxene-rich xenoliths. The samples are identified by sequential numbers with the abbreviations of MPSX-PR (Minamitorishima petit-spot xenolith peridotite) or MPSX-PX (Minamitorishima petit-spot xenolith

pyroxenite). Entire scanning electron microscope images of the xenoliths are shown in Additional file 1: Fig. S1.

MPSX-PR1 peridotite is approximately 7 mm in size. Its constituent minerals are olivine, clinopyroxene, orthopyroxene, and spinel, without visible reaction rims or mineral overgrowths derived from reaction with the host basalt (Fig. 3a). Orthopyroxenes with lamellae are larger (<1.5 mm in diameter) than the olivines and clinopyroxenes (0.1–0.7 mm in diameter). MPSX-PR2 peridotite is approximately 7 mm in size, and composed of olivine, clinopyroxene, and orthopyroxene. The olivines and orthopyroxenes range in size up to 3 mm and from 0.5 to 0.7 mm, respectively, whereas clinopyroxenes with orthopyroxene lamellae range in size from 0.2 to 1.2 mm (Fig. 3b). Thin (<10 μm in width) reaction rims are observed all around the contact part with the host basalt. A spongy texture occurs along the grain boundaries of clinopyroxenes with lamellae (Fig. 3b).

MPSX-PX1 pyroxenite (~8 mm in size) consists of coarse-grained (0.5–3 mm in diameter) clinopyroxene and orthopyroxenes with thin reaction rims in contact with the groundmass. These are surrounded partly by micrometer-sized clinopyroxenes (mainly Ti-augite of a few tens of μm), resembling those in the groundmass of the host basalt (Fig. 3c). The clinopyroxene shows spongy texture as well. MPSX-PX2 and MPSX-PX3 pyroxenites are 3 and 4.5 mm in diameter, respectively. They are mostly monocrystalline orthopyroxene accompanied by small (0.1–0.5 mm in diameter) clinopyroxenes. Needle-shaped micrometer-sized Ti-augite embedded in a glass matrix completely surrounds both samples (Fig. 3d, e).

MPSX-PX4 and MPSX-PX5 pyroxenites are approximately 5 and 9 mm in size, respectively. They are composed mainly of orthopyroxene and clinopyroxene. The clinopyroxenes are spongy textured with orthopyroxene lamellae and/or blebs (Fig. 3f, g). Ti-magnetite occur in porosities of spongy texture, and thin reaction rims observed as well (Fig. 3f, g). MPSX-PX6 clinopyroxene xenocryst (3–4 mm in diameter) has a spongy texture and a micron-sized Ti-augite rim as well (Fig. 3h).

As a whole, the petrographic characteristics of xenoliths are summarized as the following three points: (1) There are no significant petrographic differences between the two peridotite xenoliths; (2) the pyroxenites are divided into three types: clinopyroxene- and orthopyroxene-bearing aggregates, orthopyroxene lamellae/blebs in clinopyroxene, and clinopyroxene grains in orthopyroxene; and (3) the spongy texture occurred predominantly in the outer part of clinopyroxene grains, except for MPSX-PR1.

4 Analytical methods

Major-element compositions of minerals were determined using an electron probe microanalyzer (EPMA; JXA-8900R) at Atmosphere and Ocean Research Institute, the University of Tokyo. The analyses were performed using an accelerating voltage of 15 kV, a beam current of 12 nA, and a beam diameter of 3 μm . A peak counting time of 20 s and a background counting time of 10 s were used, except for Ni, for which a peak counting time of 30 s and a background counting time of 15 s were used. Natural and synthetic minerals were used as standards. The elemental mapping was also conducted using an accelerating voltage of 15 kV, a beam current of 100 nA, and a probe diameter of 15 μm dwelled at 80 ms. Each map was acquired in 1–5 h with a step size of 15 or 20 μm at resolutions ranging between 220 and 430 pixels in X by 220–500 pixels in Y . The profile analyses were performed for selected clinopyroxene grains with a step size of 5–60 μm .

The trace-element compositions of minerals were determined using a laser ablation-inductively coupled plasma mass spectrometry (LA-ICP-MS; New Wave Research UP-213 and Agilent 7500s) at Kanazawa University. The Nd: YAG deep UV (ultraviolet) laser's wavelength is 213 nm. The analyses were conducted with 100 μm spot size (Fig. 3). A repetition frequency of 6 Hz and a laser energy density of 8 J cm^{-2} were used. NIST612 glass (distributed by National Institute of Standards and Technology) was employed for calibration, using the preferred values of Pearce et al. (1997). Data reduction was undertaken with ^{29}Si as the initial standard, and SiO_2 concentrations obtained by an electron microprobe analysis (Longerich et al. 1996). BCR-2G (distributed by the United States Geological Survey) was used as a secondary standard to assess the

precision of each analytical session (Jochum and Nohl 2008).

Whole-rock major- and trace-element compositions of two basalt samples were analyzed at Activation Laboratories Ltd., Canada, using Code 4Lithoresearch Litho geochemistry Package. The package uses lithium metaborate/tetraborate fusion with inductively coupled plasma optical emission spectrometry (FUS-ICPOES) and inductively coupled plasma mass spectrometry (FUS-ICPMS) for the major- and trace-element analyses, respectively.

Raman spectra of the CO_2 fluid inclusion in pyroxene were obtained using a micro-Raman spectrum analysis system set up at the Hokkaido University Museum. Raman spectra were gained using diode-pumped solid-state laser (532 nm, Gem 532; Laser Quantum) excitation, a spectrometer with 75 cm focal length (Acton SP-2750; Princeton Instruments, Inc.), and CCD camera (1650 \times 200 pixels, 16 μm width, iVac; Andor Technology). A 50 μm core diameter multimode fiber served as the pinhole for confocality and as the entrance slit to the spectrometer. The laser was focused through a 50 \times objective (N.A. = 0.8, LUPlan; Nikon Corp.) with working distance of approximately 1.0 mm. The laser output was 50 mW at the source and approximately 8.0 mW at the sample surface. The wavenumber dispersion for each pixel of the present Raman system when using a grating of 1,800 lines/mm is 0.29 cm^{-1} /pixel at around 1334 cm^{-1} . Raman spectra were collected with two to four accumulations of 100 s.

A Raman CO_2 densimeter was applied to estimate the density of CO_2 fluid inclusions. This analysis used the density dependence of Fermi diad splits (Δ) of CO_2 fluid, and we applied the Δ –density relation of Hagiwara et al. (2020). To measure Δ with high accuracy, real-time wavenumber calibration was applied to reduce the deviation of Raman frequency (Odake et al. 2008). As described by Hagiwara et al. (2020), the measured Δ was calibrated by using the measured and known (227.46 cm^{-1}) distances between the Ne lines according to the following expression:

$$\Delta_{\text{real}}^{\text{corrected}} = \Delta_{\text{mes}}^{\text{CO}_2} \times \left(\frac{227.46}{\Delta_{\text{mes}}^{\text{Ne}}} \right)$$

In this equation, $\Delta_{\text{real}}^{\text{corrected}}$ denotes the corrected splitting of the Fermi diad, $\Delta_{\text{mes}}^{\text{Ne}}$ represents the measured separation between the 1,449.19 and 1221.73 cm^{-1} Ne emission lines, and $\Delta_{\text{mes}}^{\text{CO}_2}$ stands for the measured splitting of Δ in the Raman spectrum. The measured spectra for CO_2 and Ne lines were fitted with the GRAMS AI program, respectively, using a Gaussian and Lorentzian mixture and a Lorentzian function. More than 500 counts of the Fermi diad band at 1386 cm^{-1} are necessary to

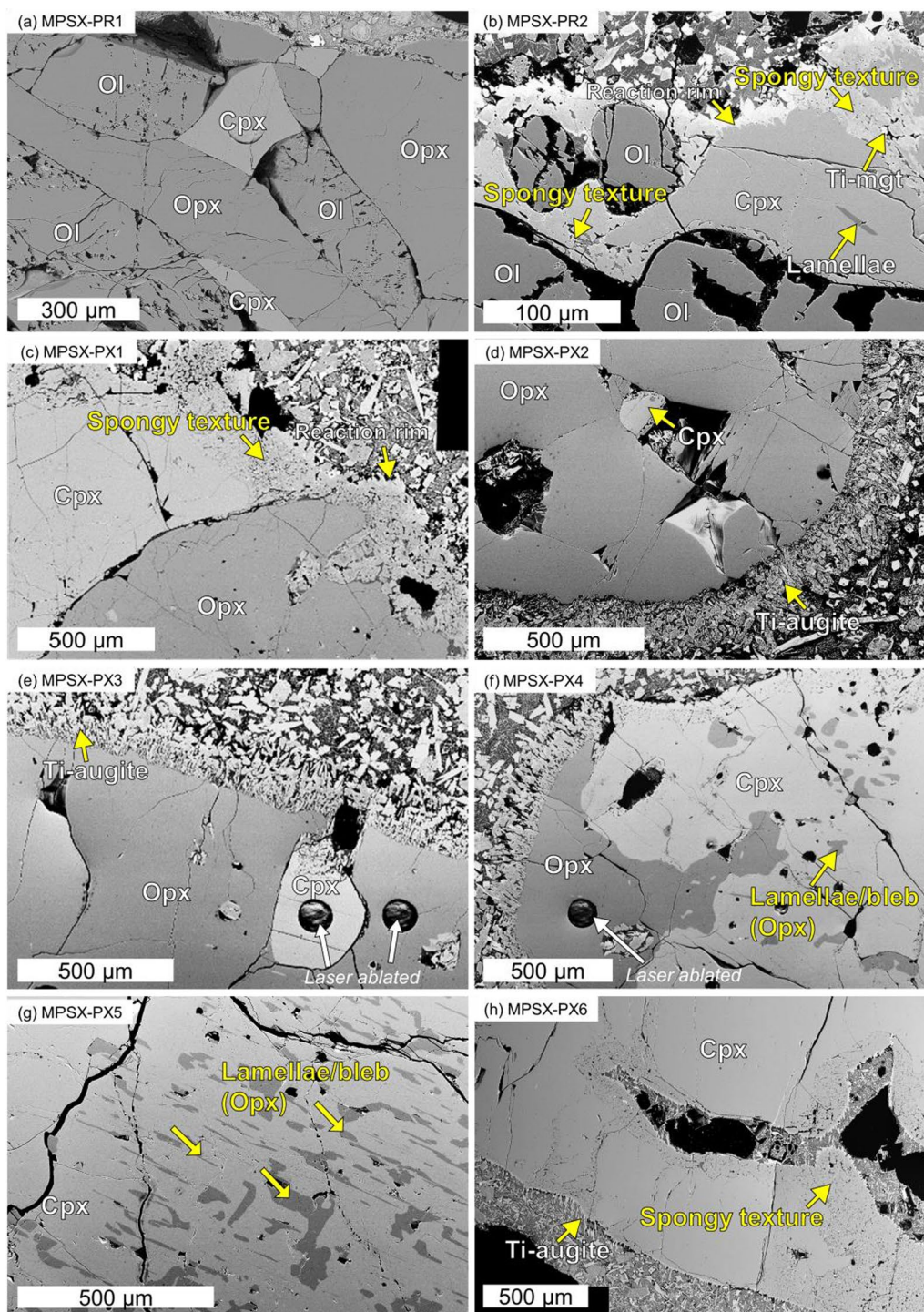


Fig. 3 Scanning electron microscope images of the samples. **a** MPSX-PR1 peridotite, **b** MPSX-PR2 peridotite, **c** MPSX-PX1 pyroxenite, **d** MPSX-PX2 pyroxenite, **e** MPSX-PX3 pyroxenite, **f** MPSX-PX4 pyroxenite, **g** MPSX-PX5 pyroxenite, and **h** MPSX-PX6 clinopyroxene xenocryst

obtain a delta (Δ) value with high precision (within 1σ of 0.03 cm^{-1}) for the present system (Kawakami et al. 2003), and then, we use the data more than 500 counts. To correct the discrepancy in the Δ -density relations derived

in earlier studies, we applied the correction method proposed by Hagiwara et al. (2020). In this method, a correction term δ is added to $\Delta_{\text{real}}^{\text{corrected}}$ to estimate the density accurately using the Δ -density relation of Hagiwara et al.

(2020). To calculate the correction term δ , the two standard fluid inclusions with densities of 0.914 and 1.167 g/cm³ were used. See Hagiwara et al. (2020) for detailed methods. The conversion from obtained density to pressure of CO₂ fluid inclusion was conducted using the equation [2] and [4] from Pitzer and Sterner (1995). Note that the peaks except for CO₂ (i.e., N₂, H₂S, CO, SO₂, and CH₄) were below the detection limit. Moreover, considering the room temperature (23 °C), laser power (8 mW), and the temperature increase in inclusions per unit laser power (1 °C/mW for pyroxene at 532 nm) (Hagiwara et al. 2021), the inclusion temperature exceeded the supercritical temperature of CO₂, indicating that CO₂ was in a single phase during the analysis. See the supplementary information of Yamamoto et al. (2014) for the detailed description about this geobarometry.

5 Results

5.1 Basalt chemistry

The host basalts are silica-undersaturated foidite (i.e., 39.7–40.2 wt% SiO₂, and 3.9–4.4 wt% total alkalis [Na₂O + K₂O]) (Fig. 4a). Trace-element patterns of the foidites are similar to petit-spot basalts reported by Hirano et al. (2006), Machida et al. (2015), and Sato et al. (2018) (Fig. 4b) in particular Zr, Hf, and Ti negative anomalies. Detailed values are provided in Table 1.

5.2 Major-element composition of minerals

Olivines in MPSX-PR1 peridotite show forsterite content (Fo#: Mg# = $100 \times \text{Mg}^{2+}/[\text{Mg}^{2+} + \text{Fe}^{2+}]$ for olivine) of 90.5–91.0 and NiO concentrations of 0.36–0.40 wt% (Fig. 5a). Clinopyroxenes and orthopyroxenes of MPSX-PR1 display the highest Mg# of 92.7–93.4 and 90.7–91.6, respectively, within ultramafic xenoliths in this study (Fig. 5b, c). The TiO₂ and Al₂O₃ concentrations of clinopyroxene in MPSX-PR1 are the lowest, 0.05–0.16 wt% and 1.7–2.0 wt%, respectively, with a high Cr₂O₃ content of 0.94–1.06 wt% (Fig. 5c, d). The orthopyroxene Al₂O₃ contents are low, 1.4–1.7 wt%, whereas the CaO concentrations have a wide range of 0.73–2.5 wt%. Chromian spinels are found only in MPSX-PR1, showing Cr# ($100 \times \text{Cr}^{3+}/[\text{Cr}^{3+} + \text{Al}^{3+}]$) of 60.1–62.7 and Mg# of 52.9–64.8. As for MPSX-PR2 peridotite, olivines represent lower Fo# (88.1–88.7) and similar NiO content (0.33–0.41 wt%) relative to those in MPSX-PR1 (Fig. 5a). Clinopyroxenes in MPSX-PR2 have lower Mg# and higher TiO₂ concentrations of 81.9–87.0 and 1.00–1.62 wt%, respectively, than those of MPSX-PR1 (Fig. 5c). Although the Al₂O₃ content of clinopyroxenes is higher than that in MPSX-PR1 (4.6–6.9 wt%), Cr₂O₃ concentrations have similar values of 0.87–1.14 wt% (Fig. 5d). The Mg#, Al₂O₃, and CaO contents of orthopyroxene are 88.2–89.2, 2.3–4.9 wt%, and 1.1–1.2 wt%, respectively.

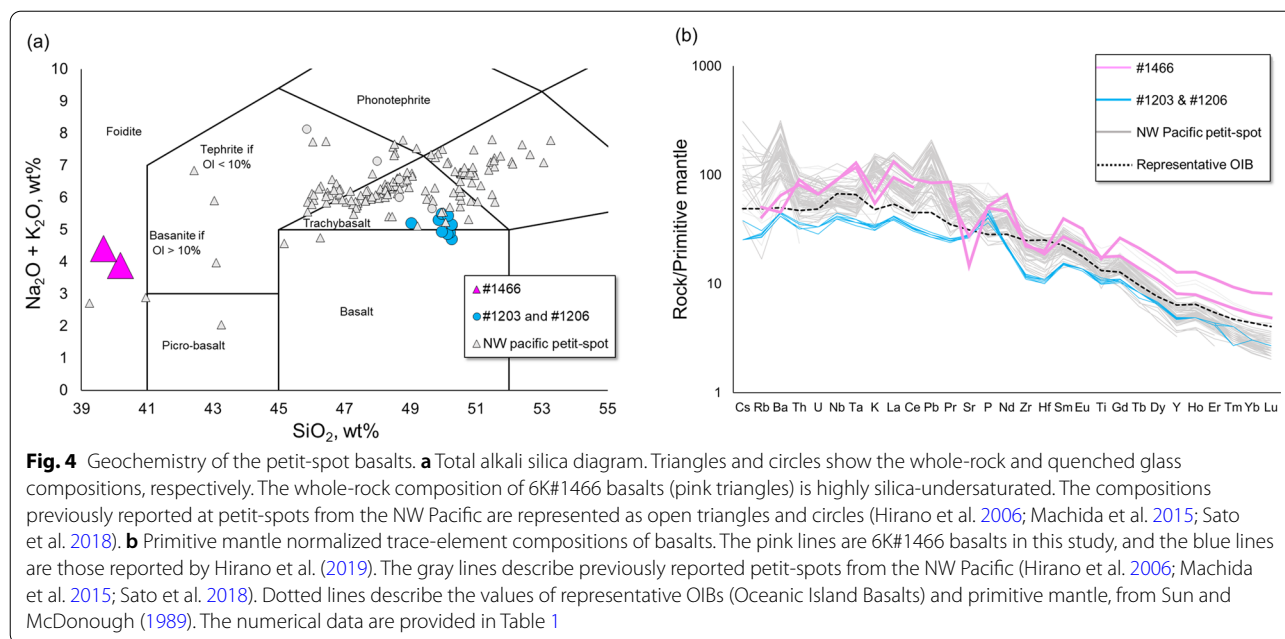
The geochemical characteristics of pyroxenite xenoliths and pyroxene xenocrysts (MPSX-PX1 to MPSX-PX6 and isolated xenocrysts) are similar to each other. Clinopyroxenes have lower Mg# and higher TiO₂ concentrations of 72.6–79.8 and 0.59–1.61 wt%, respectively, compared to the peridotite xenoliths in this study (Fig. 5c). The Al₂O₃ content of clinopyroxene shows a wide range, of 3.7–7.5 wt%, resembling MPSX-PR2, whereas Cr₂O₃ contents of 0–0.27 wt% are generally lower than those of the two peridotites (Fig. 5d). The Mg#, Al₂O₃, and CaO contents of orthopyroxene are 76.3–80.3, 2.5–5.1 wt%, and 1.4–2.1 wt%, respectively. Orthopyroxene lamellae and indeterminate-shaped orthopyroxenes in the clinopyroxene host phase of MPSX-PX4 and MPSX-PX5 all have similar compositions. The average compositions of isolated clinopyroxene xenocrysts were 72.7 Mg#, 1.46 wt% TiO₂, 7.2 wt% Al₂O₃, and 0.06 wt% Cr₂O₃.

In summary, pyroxenite xenoliths and pyroxene xenocrysts in this study have more fertile compositions than MPSX-PR1 peridotite, and some elements resemble the clinopyroxene concentrations in MPSX-PR2 peridotite. Detailed values are given in Additional file 4: Tables S1 to S4.

We focused on Ca and Al variation in the line profile and the elemental mapping for clinopyroxene (Fig. 6). The clinopyroxene rim in MPSX-PR1 shows slightly higher Ca and lower Al than the homogeneous inner part (Fig. 6a). From MPSX-PR2 Cpx#1 to MPSX-PX6, clinopyroxenes tend to show an increase for Ca and a decrease for Al in spongy textures, while both Ca and Al tend to increase at the outermost rims (where they are in contact with host groundmass), but these areas are heterogeneous (Fig. 6b–i). The clinopyroxene grain of MPSX-PX2 is surrounded by orthopyroxene and does not represent the reaction texture, but gradual zonings for Al are identified (Fig. 6e). The reaction rim including the outermost rim and the spongy texture of MPSX-PX5 is relatively thin (< 90 μm), but Ca becomes more pronounced at the rim, while Al is variable (Fig. 6h). Simultaneously, although MPSX-PX5 shows compositional heterogeneity according to the distribution of orthopyroxene lamellae, the core has a different composition from the reacted portions (Fig. 6h).

5.3 Trace-element composition of clinopyroxenes

Primitive mantle normalized trace-element patterns for the clinopyroxene core in this study are shown in Fig. 7a. The previously reported data of abyssal peridotites and xenoliths in Pacific hotspots and NW Pacific petit-spot lavas are also available in Fig. 7a, b. The MPSX-PR1 peridotite generally resembles abyssal peridotite from the East Pacific Rise (EPR) Hess Deep, with



a low LREE/heavy-rare-earth element (HREE) ratio (Dick and Natland 1996; Regelous et al. 2016; Warren 2016). In contrast, clinopyroxene patterns in the MPSX-PR2 peridotite, pyroxenites, and pyroxene xenocrysts (MPSX-PX1, MPSX-PX3, MPSX-PX4, and isolated clinopyroxenes) show higher LREE/HREE ratios than that of MPSX-PR1 (i.e., high enrichment of LREE). The absolute concentrations of incompatible elements between the fertile series (MPSX-PR2 peridotite and pyroxenite xenoliths) and depleted peridotite (MPSX-PR1) are clearly different as well. The MPSX-PR2 peridotite notably shows negative anomalies in Zr, Hf, and Ti, which are not shown in the pyroxenite series and pyroxene xenocrysts. The concentrations of U, Th, Nb, and Ta are higher in the MPSX-PR2 clinopyroxenes than in the pyroxenite xenoliths and pyroxene xenocrysts. Detailed values are provided in Additional file 4: Tables S5 and S6.

5.4 Geothermobarometry

Equilibrium temperatures were obtained using the two-pyroxene thermometer formulated by Brey and Köhler (1990) for samples including both orthopyroxene and clinopyroxene. The equilibrium temperatures at core part of two-pyroxenes are 977 ± 62 °C for MPSX-PR1 peridotite, 1069 ± 85 °C for MPSX-PR2 peridotite. Most pyroxenites show similar temperatures of 1076 ± 41 °C for MPSX-PX1, 1053 ± 16 °C for MPSX-PX2, 1073 ± 25 °C for MPSX-PX3, and 1093 ± 17 °C for MPSX-PX4, but MPSX-PX5 shows higher temperature of 1157 ± 50 °C. We use these values to calculate the residual pressures of CO₂ inclusion for two peridotites and two pyroxenites

(MPSX-PX1 and PX5). The K_D values $[=(X_{Fe}^{cpx}/X_{Mg}^{cpx})/(X_{Fe}^{opx}/X_{Mg}^{opx})]$ are within the equilibrium range of 1.09 ± 0.14 proposed by Putirka (2008), but MPSX-PR1 has a small offset ($K_D = 0.762$).

Residual pressures were estimated by adopting the densimeter of CO₂ fluid inclusions in the pyroxenes. The pressures calculated from the density of CO₂ fluid inclusions with two-pyroxene temperatures are 0.410 ± 0.006 GPa for MPSX-PR1 peridotite, 0.902 ± 0.005 GPa for MPSX-PR2 peridotite, 0.620 ± 0.008 GPa for MPSX-PX1 pyroxenite, and 1.197 ± 0.002 GPa for MPSX-PX5 pyroxenite. The pressures obtained were converted to seafloor depths; the resulting temperature–depth and pressure diagram is shown as Fig. 8a. A detailed account of the validation of this geobarometry for the mantle xenolith is given later (the first paragraph in Sect. 6.3). Imagery of a fluid inclusion and Raman shift is provided in Additional file 2: Fig. S2. Detailed parameters and all obtained values are given in Table 2 and S7. The equilibrium temperatures and pressures for ultramafic xenoliths were also calculated using the two-pyroxene geothermobarometer of Putirka (2008). The calculated temperatures and pressures are 1011 ± 56 °C and 0.37 ± 0.08 GPa for MPSX-PR1 peridotite, and 1100 ± 21 °C and 0.76 ± 0.16 GPa for MPSX-PR2 peridotite. The range of temperature and pressure for five pyroxenite xenoliths is 1078–1109 °C and 0.82–1.07 GPa. The depth–temperature diagram for these values is also shown as Fig. 8b. We use the average core composition of pyroxenes. In particular, the temperature of MPSX-PX5 pyroxenite was applied to the average composition of the most homogeneous part

Table 1 Major and trace element composition of petit-spot basalts

Cruise	YK16-01	YK16-01
Dive	6K#1466	6K#1466
No	R7-001	R7-003
wt%		
SiO ₂	39.40	39.27
Al ₂ O ₃	11.41	11.46
Fe ₂ O ₃ (T)	16.80	16.56
MnO	0.21	0.20
MgO	9.34	7.66
CaO	11.19	10.02
Na ₂ O	2.15	2.29
K ₂ O	1.65	2.08
TiO ₂	3.82	3.68
P ₂ O ₅	1.08	1.12
Total	99.73	100.60
Mg#	52.42	47.82
K ₂ O/Na ₂ O	0.77	0.91
LOI	2.68	6.29
μg/g		
Sc	25	25
Be	2	2
V	353	324
Ba	453	317
Sr	577	307
Y	37	58
Zr	259	248
Cr	200	190
Co	61	57
Ni	200	140
Cu	90	90
Zn	180	200
Ga	20	18
Ge	1	2
As	<5	5
Rb	26	32
Nb	65	64
Mo	2	<2
Ag	0.8	1
In	<0.2	<0.2
Sn	2	2
Sb	<0.5	0.6
Cs	<0.5	<0.5
La	65.2	90.8
Ce	138	164
Pr	16.6	23.8
Nd	62.6	89.3
Sm	12	17.6
Eu	3.76	5.38
Gd	10.7	15.7
Tb	1.5	2.3

Table 1 (continued)

Cruise	YK16-01	YK16-01
Dy	8	12.2
Ho	1.3	2.1
Er	3.3	5.3
Tm	0.44	0.69
Yb	2.6	4.1
Lu	0.36	0.6
Hf	5.8	6.2
Ta	4.8	5.3
W	<1	<1
Tl	0.8	0.3
Pb	<5	6
Bi	<0.4	<0.4
Th	6.9	7.7
U	1.4	1.4

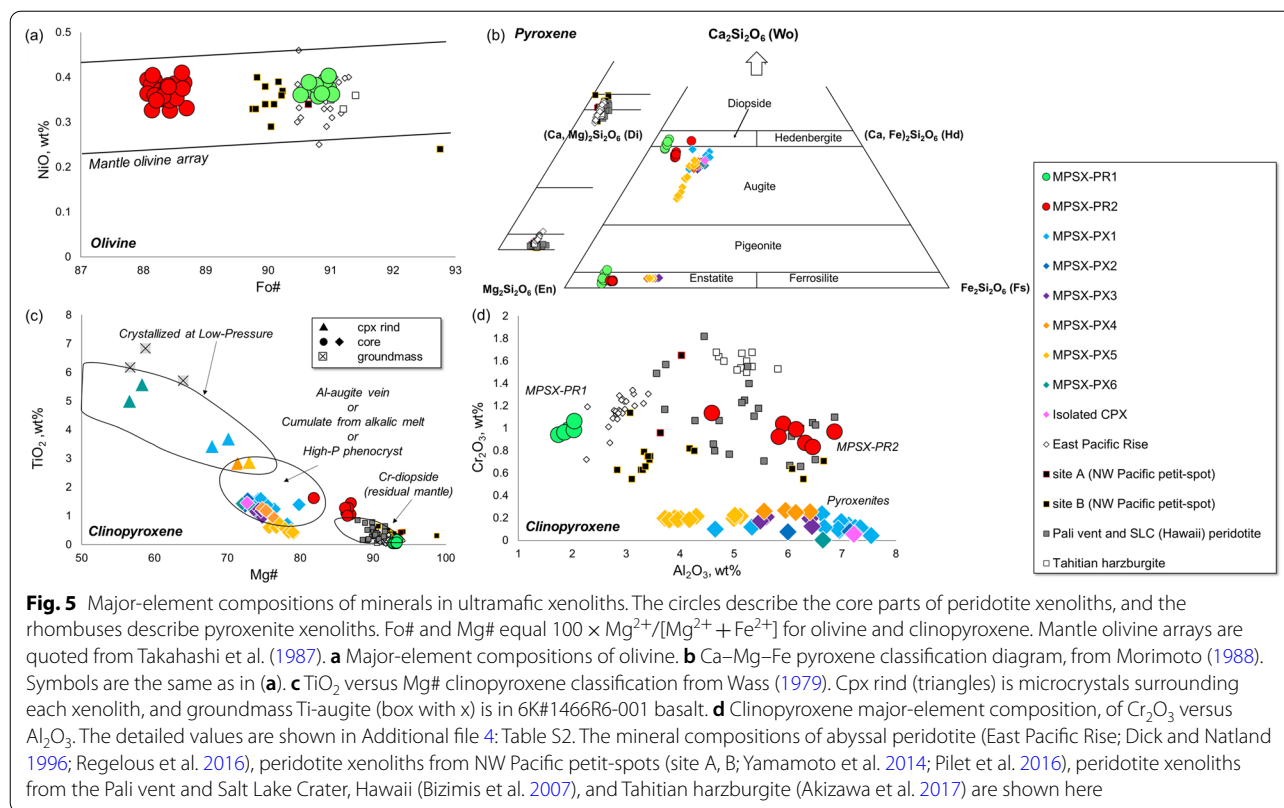
of the clinopyroxene and orthopyroxene blebs (Fig. 6h). Detailed values are given in Table 2. The method of error calculation for this thermobarometry is described in Additional file 3.

6 Discussion

6.1 The origins of xenolith

Ultramafic xenoliths in intraplate volcanoes can be divided into Cr-diopside series or Al-augite series, depending on the clinopyroxene composition (Wilshire and Shervais 1975; Wass 1979). The former is interpreted as a residue after crust production at the spreading center, including Cr-rich spinels, Mg-rich orthopyroxenes, and Mg-rich olivines. Conversely, the latter has three conceivable origins as metasomatic vein formed by melt–peridotite reaction, phenocryst crystallized at high pressure, or a cumulate from alkali basaltic melt, composed of Al-rich spinels, Fe-rich orthopyroxenes, and Fe-rich olivines. Cr-diopside series xenoliths generally show the depletion of incompatible elements, but sometimes have enriched composition modally or cryptically (e.g., a high LREE/HREE ratio; Dawson 1984). In addition, ultramafic xenoliths often represent higher equilibrium temperatures than those expected by the underlying pristine oceanic lithosphere (Hauri and Hart 1994; Qi et al. 1994). Such features often suggest local lithospheric modifications resulted from intraplate magma infiltrations.

MPSX-PR1 and MPSX-PR2 peridotites have high Cr₂O₃ contents in clinopyroxenes (Fig. 5d). However, other chemical features of these two peridotites are significantly different. In the pyroxene quadrilateral diagram (Fig. 5b), the clinopyroxenes in MPSX-PR1 peridotite are classified as diopside and those in MPSX-PR2 peridotite are classified as augite. The fayalite component of olivine



and the TiO_2 , Al_2O_3 , and iron contents of clinopyroxene are higher in MPSX-PR2 peridotite than those in MPSX-PR1 peridotite (Fig. 5b–d). The Mg# and Al_2O_3 contents of the orthopyroxenes also differ: The higher Al_2O_3 and lower Mg# of MPSX-PR2 as compared with MPSX-PR1 indicate that MPSX-PR2 peridotite is more fertile than MPSX-PR1. The mineral compositions of MPSX-PR1 peridotite and the other Pacific oceanic peridotites are similar to each other with the exception of the Al_2O_3 and Cr_2O_3 contents of clinopyroxene (Fig. 5). The variation of clinopyroxene Al_2O_3 contents in the other Pacific peridotite xenoliths could be explained by the degree of fertilization (Bizimis et al. 2007; Yamamoto et al. 2014; Pilet et al. 2016; Akizawa et al. 2017). Based only on the above, we can estimate that MPSX-PR1 peridotite originates from residual mantle with highly depleted Cr# of chromian spinels (60.1–62.7; Additional file 4: Table S4) (cf., < 60.6 Cr# in Hess Deep peridotites: Arai and Matsukage, 1996; Dick and Natland, 1996). By contrast, MPSX-PR2 peridotite is derived from fertilized mantle and its protolith might be Cr-diopside series depleted peridotite.

The primitive mantle normalized trace-element patterns of the clinopyroxenes in MPSX-PR1 peridotite shows low LREE/HREE ratios, overlapping the composition of residual harzburgites from the Hess Deep, EPR (Dick and Natland 1996; Regelous et al. 2016; Warren

2016) (Fig. 7a). Even some LREE-depleted peridotites reported from the Ka’au vent and the Pali vent in Hawaii (Sen et al. 1993) are not as depleted in LREE as those of the EPR (Fig. 7b). In contrast, clinopyroxenes in MPSX-PR2 peridotite are marked by relative enrichment in LREE, resembling those of metasomatized peridotites reported from the NW Pacific petit-spot (Pilet et al. 2016) (Fig. 7a). Additionally, all xenoliths in this study are suggested to originate from spinel-stability field, based on their trace-element patterns (i.e., the absence of HREE depletion; Fig. 7a) and thermobarometry (Fig. 8). This finding is conflict with NW Pacific mantle xenoliths where the trace-element patterns indicate both garnet- and spinel-stability field origins (Pilet et al. 2016) (Fig. 7a). Moreover, enriched MPSX-PR2 peridotite shows the negative anomalies of Zr, Hf, Ti, Sr, and Nb as well as the metasomatized Tahitian harzburgite xenolith and some enriched Hawaiian peridotite xenoliths (Fig. 7b; Bizimis et al. 2005, 2007; Akizawa et al. 2017). This also suggests that the enriched peridotite (MPSX-PR2) is of metasomatic origin. As discussed below, we expect that pyroxenites, which show a similar trace-element composition to those of enriched peridotite (MPSX-PR2), were also formed by magma–lithospheric mantle interaction.

In summary, we suggest that MPSX-PR1 peridotite corresponds to a depleted harzburgite left after melt

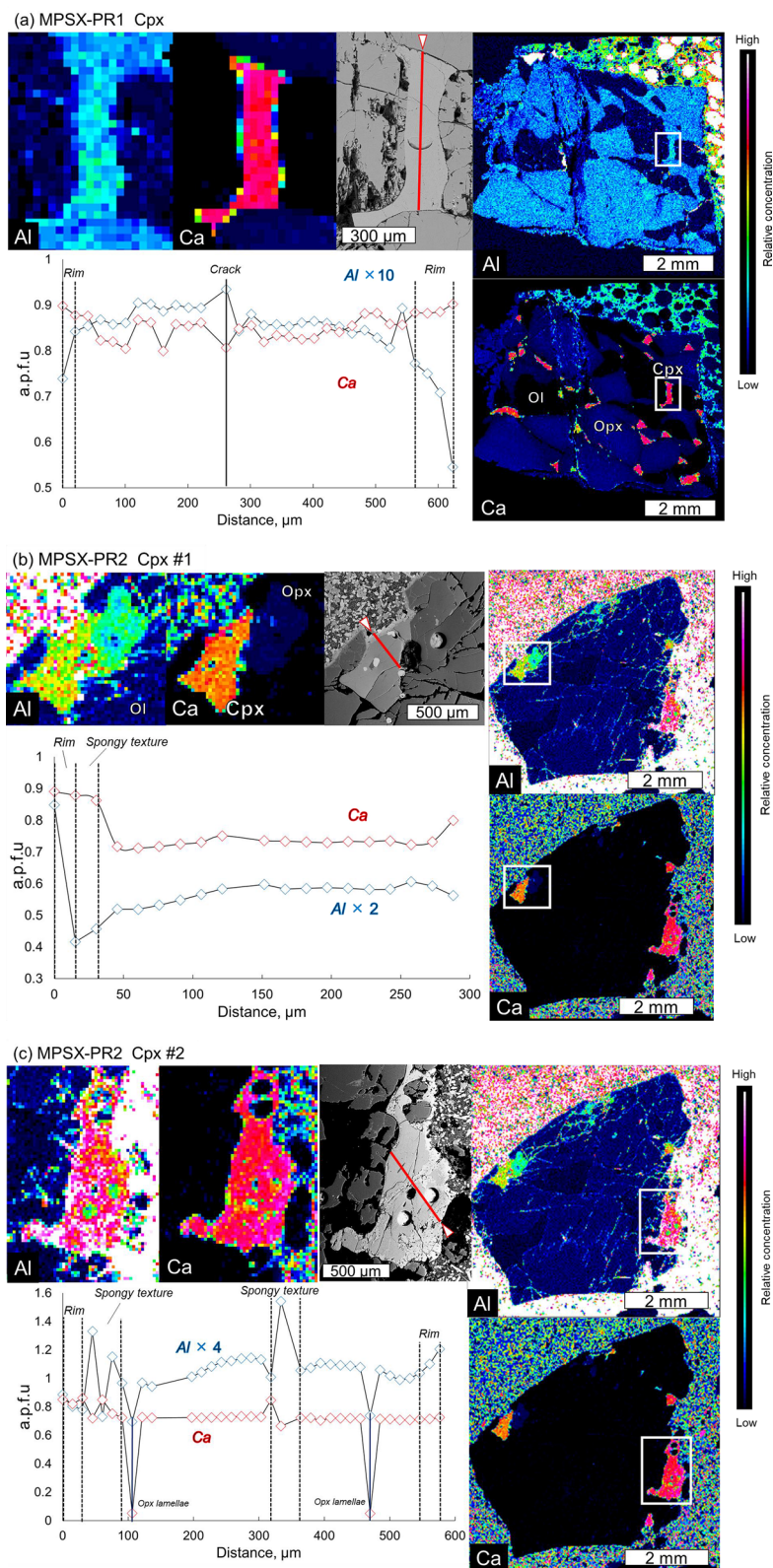


Fig. 6 Elemental mappings of xenolith and line profiles of clinopyroxene for Ca and Al. The red lines on the backscattered electron image and white lines on the elemental map are the analyzed lines. Triangle symbols indicate the starting points. In the a.p.f.u (atoms per formula unit) vs. distance diagram, the red and blue diamonds display Ca and Al cation numbers, respectively. The cation numbers for Al are multiplied by a constant for ease of viewing. **a** MPSX-PR1. **b**, **c** MPSX-PR2. **d** MPSX-PX1. **e** MPSX-PX2. **f** MPSX-PX3. **g** MPSX-PX4. **h** MPSX-PX5. **i** MPSX-PX6

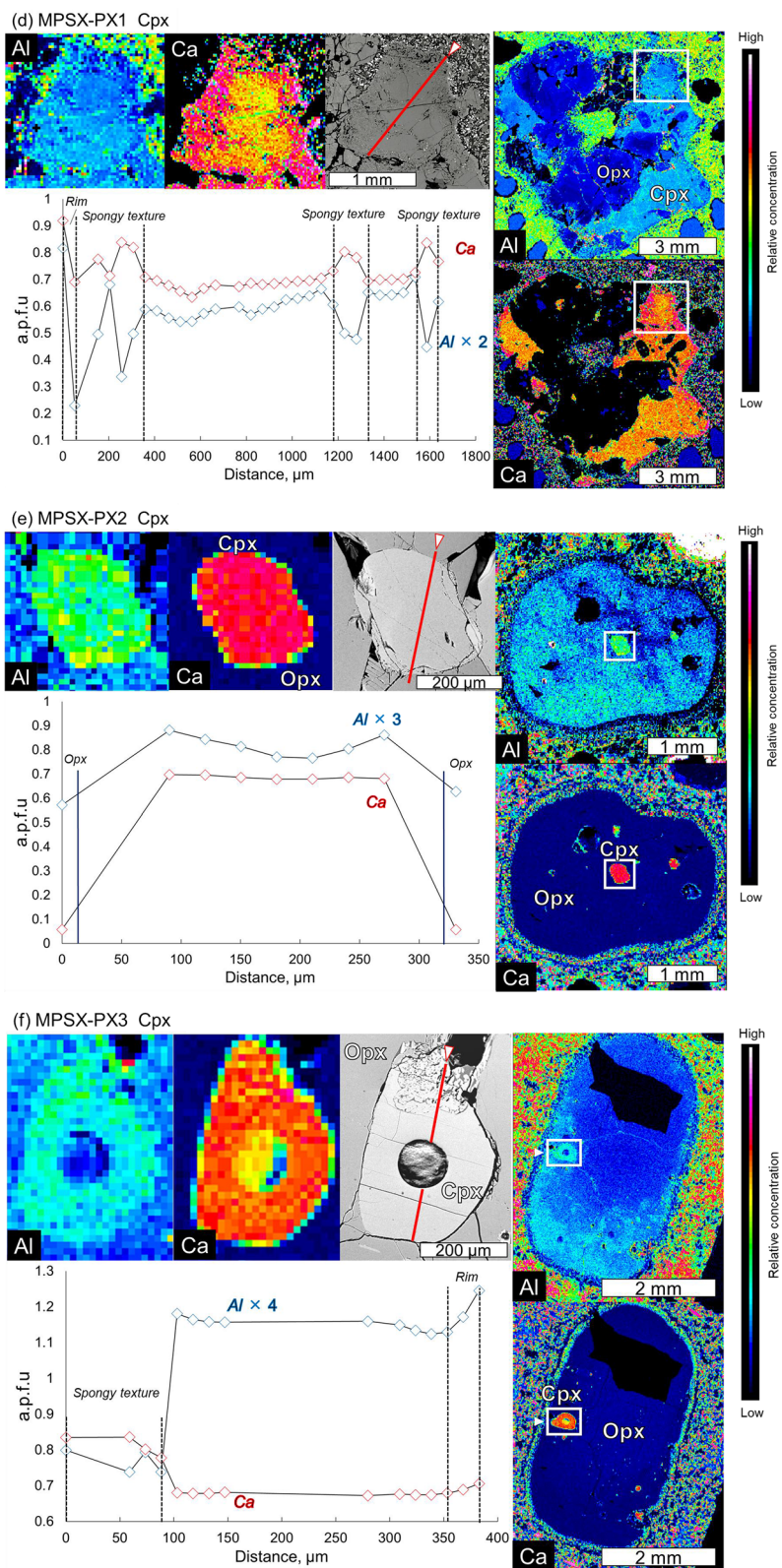


Fig. 6 continued

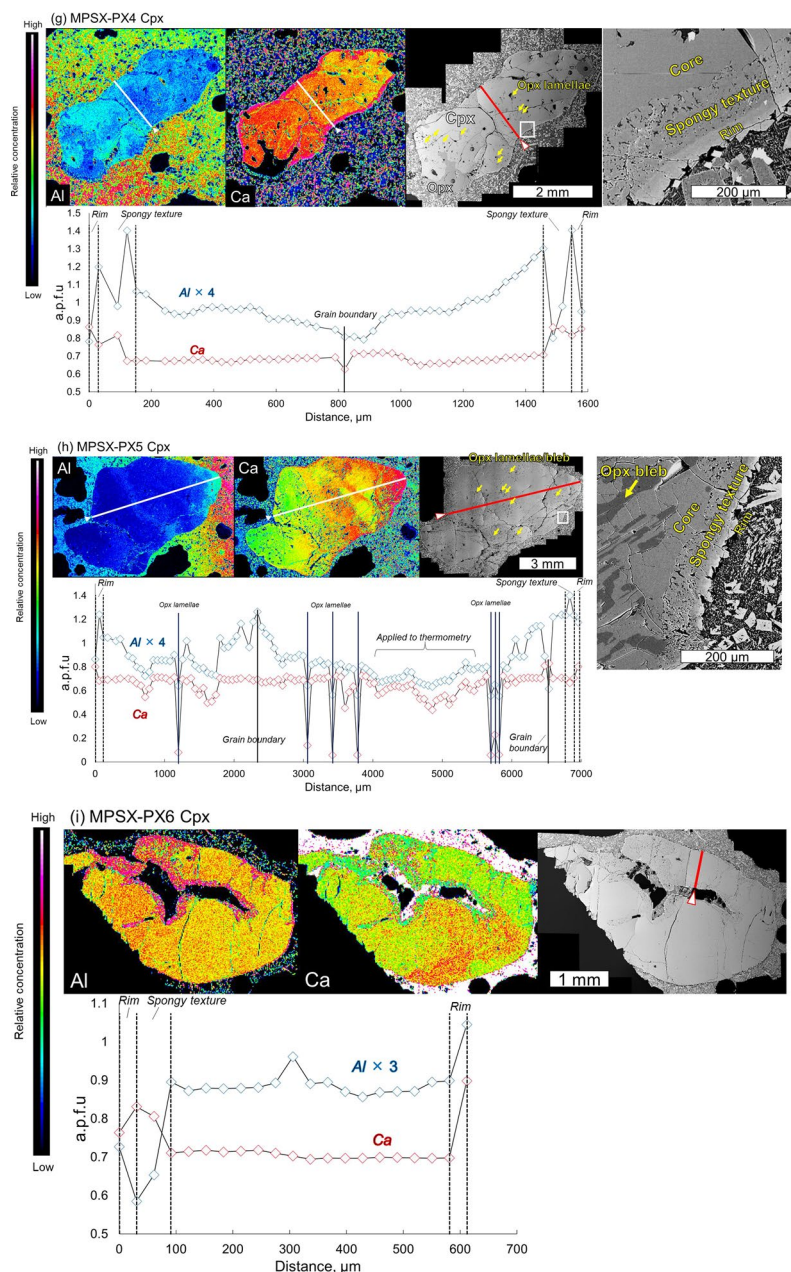
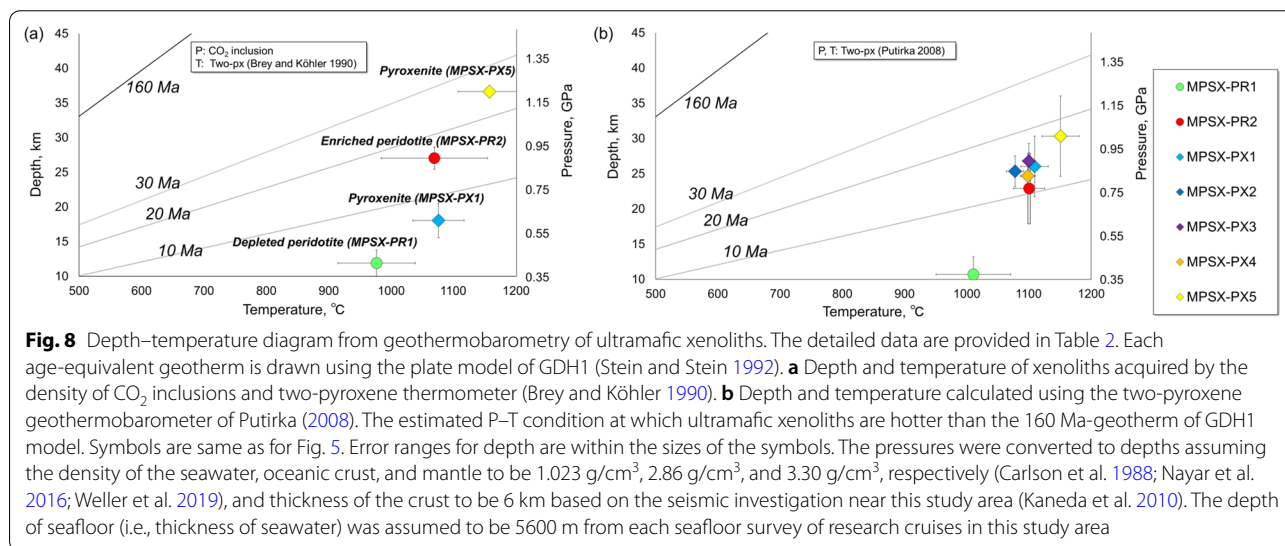
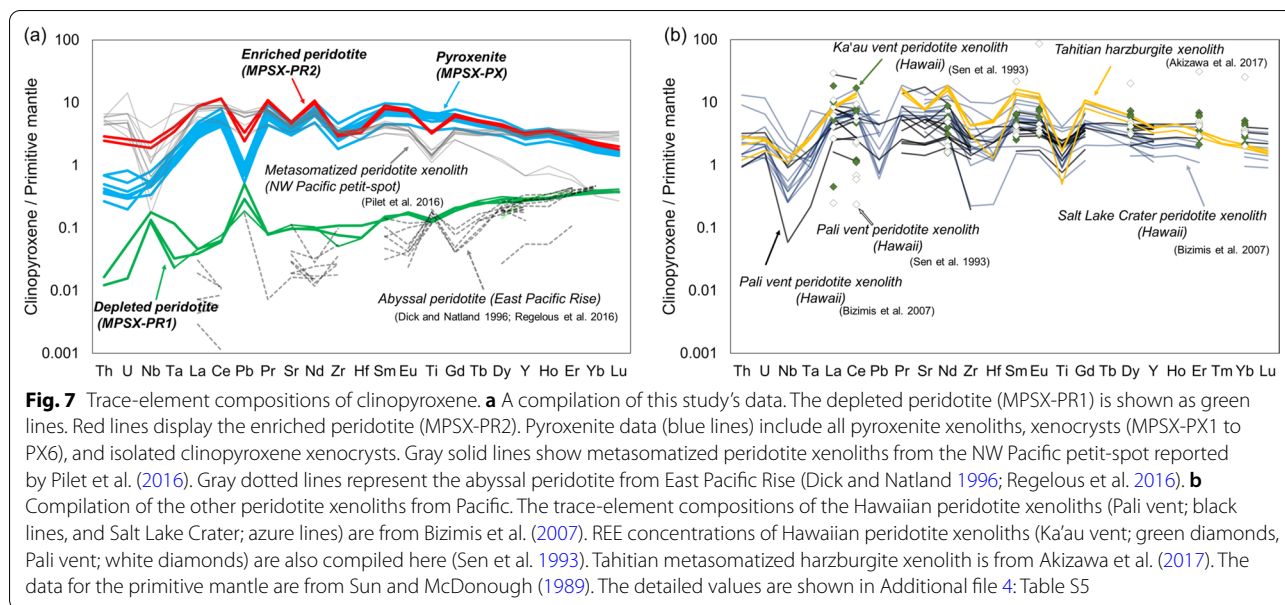


Fig. 6 continued

extraction, whereas MPSX-PR2 peridotite is a metasomatized mantle fragment by intraplate magmatism. We propose this metasomatic agent could be previous petit-spot magmatism as discussed later.

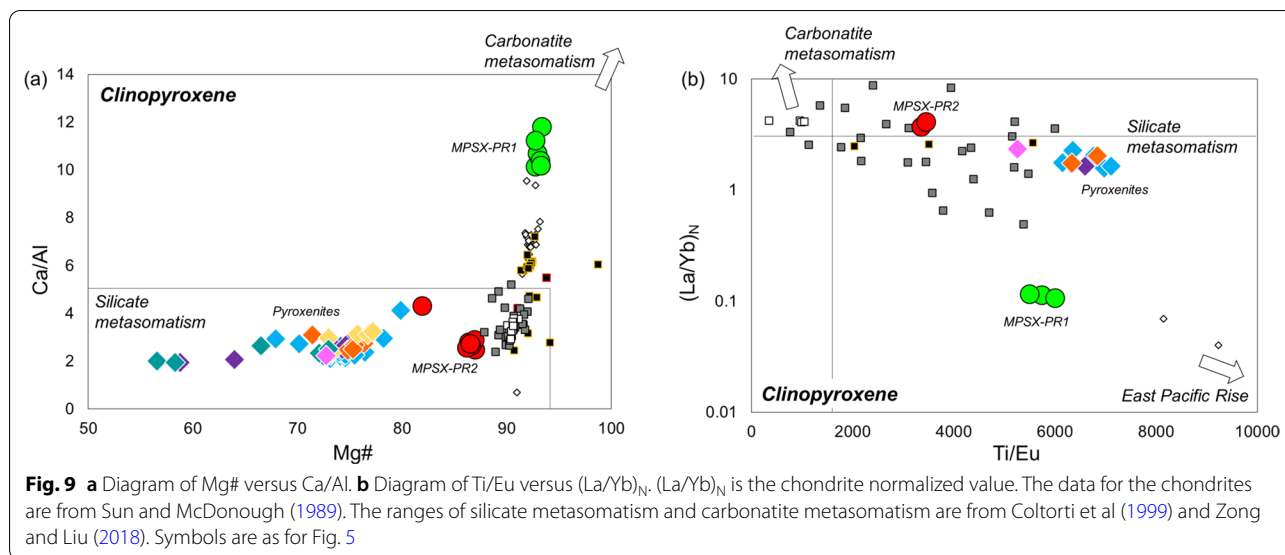
Pyroxenite xenoliths (MPSX-PX1 to MPSX-PX5), the clinopyroxene xenocryst (MPSX-PX6), and isolated (handpicked) clinopyroxene xenocrysts are similar composition and all categorized as Al-augite series, considering that clinopyroxene Cr_2O_3 contents are low

(0–0.28 wt%) and Al_2O_3 contents are high (Fig. 5b, d) and orthopyroxenes are rich in Fe and Al (Fig. 5b). The chemical characteristics are obviously different from the two peridotites, as shown in Fig. 5a–d. The cores of the MPSX-PX6 augite xenocryst and other isolated clinopyroxene xenocrysts are similar in compositions to clinopyroxenes in pyroxenite xenoliths (Figs. 5b–d, 7), implying their same origin. Among the three conceivable origins of Al-augite series pyroxenite xenoliths as described



above, this study samples plausibly originate from metasomatic veins to explain their petrographic features as follows (Wass 1979) (Fig. 5c): (1) The existence of bleb-like orthopyroxene lamellae in the clinopyroxene grains (Fig. 3f, g) implies a growth of exsolved orthopyroxene for a relatively long period under an isothermal condition and cooling (e.g., Toh and Shimobayashi 2000; Liang et al. 2018). (2) The spongy texture in rims or grain boundaries of clinopyroxene (Fig. 3) suggests disequilibrium with the host magma (e.g., Shaw et al. 2006; Su et al. 2011). (3) Micro-Ti-augite grains around xenoliths (Fig. 3), having the similar composition as those in the ground-mass, are crystallized after entrapment in low-pressure

conditions (Fig. 5c). The compositional modification of the lithospheric mantle due to melt–rock interactions is indicated by Al-augite series xenoliths as seen in various oceanic islands/seamounts (e.g., Tracy 1980; Fodor et al. 1982; Qi et al. 1994). Moreover, fertile pyroxene-rich veins formed by interactions between alkali basaltic melt and lithospheric mantle have been proposed (e.g., Wilshire and Shervais 1975). Given the absence of olivine in our pyroxenites, it is expected that the pyroxenites were formed by the process of olivine dissolution and pyroxene formation (i.e., $Liq1 + Ol \rightarrow Cpx + Opx + Liq2$). This pyroxenite-formation process is proposed to have taken place in oceanic upper mantle (Laukert et al. 2014).



The diagram of Mg# vs. Ca/Al and Ti/Eu vs. $(La/Yb)_N$ for clinopyroxenes suggests strongly that the metasomatized mantle xenoliths in this study were metasomatized by silicate magma rather than carbonatitic magma (Fig. 9a, b). Given that it has been proposed that silicate metasomatism transforms peridotite to websterite (pyroxenite) and orthopyroxenite by consuming olivine, our olivine-free pyroxenites are expected to have been formed by silicate melt–mantle rock interaction instead of carbonatite metasomatism with orthopyroxene consumption and formation of clinopyroxene-rich lherzolite or wehrlite (e.g., Laurora et al. 2001). In addition, such fertile pyroxenite xenoliths often show higher equilibrium temperatures than might be expected from pristine geotherm on the basis of plate age in correlation with LREE concentrations as found in our samples (e.g., Hauri and Hart 1994; Burnard et al. 1998).

All of these lines of evidence indicate that the pyroxenite xenoliths in this study originated from metasomatic veins in the lithospheric mantle.

6.2 Identification of the metasomatic agent

In our study area, there are several candidates for the triggering of the metasomatic event: (1) off-axis magmatism near the mid-ocean ridge (e.g., Seyler et al. 2001; Rochat et al. 2017), (2) Cretaceous intraplate magmatism (100–120 Ma, Koppers et al. 2003; Aftabuzzaman et al. 2021), (3) irregular volcanism on the Cretaceous edifice of Minamitorishima Island at approximately 40 Ma (Hirano et al. 2021), (4) petit-spot magmatism before the xenoliths–host magma event, and (5) host magma. Among these, previous (prior to xenolith entrapment) petit-spot magmatism most

reasonably explains our results because of the high equilibrium temperature of the metasomatized xenoliths (~1100–1200 °C).

According to the study of numerical simulation about relationships between heating/cooling rates and elemental diffusion in two-pyroxene of mantle xenolith, it takes 5 to 6 million years for a clinopyroxene of ~700 °C (the condition when the elemental diffusion of clinopyroxene is halted) to reach 1300 °C (near the estimated potential temperature of the petit-spot; Machida et al. 2017) in a heating process at the rate of 10^{-4} °C/yr with the creation of gradual compositional zoning or without zoning (Yamamoto et al. 2017). Moreover, a clinopyroxene of 1300 °C takes only 1–2 million years to reach 1100 °C without creating notable compositional zoning even assuming a slow cooling rate of 10^{-4} °C/year (Yamamoto et al. 2017). As for the clinopyroxenes in the metasomatic pyroxenites, showing an equilibrium temperature of ~1100 °C without compositional zoning or with gentle zoning (Fig. 6b–i), these are expected to have experienced a similar heating/cooling processes to that described above. Additionally, if the pyroxenites in this study were formed in such a process, it would be required a total heating/cooling time of 6–8 million years just prior to entrapment. Given the relation of the cooling period to the timing of the host magmatism (0.2–5.2 Ma), volcanism at ~40 Ma, Cretaceous hotspots, and off-axis magma infiltration are unsuitable as a metasomatic agent. The ascending time of general petit-spot melts (a few hundred days; Sato et al. 2018) also rules out the host magma as a metasomatic agent because our fertile xenoliths (MPSX-PR2 and MPSX-PX1–6) have no steep elemental zoning. In addition, they show a remarkable compositional

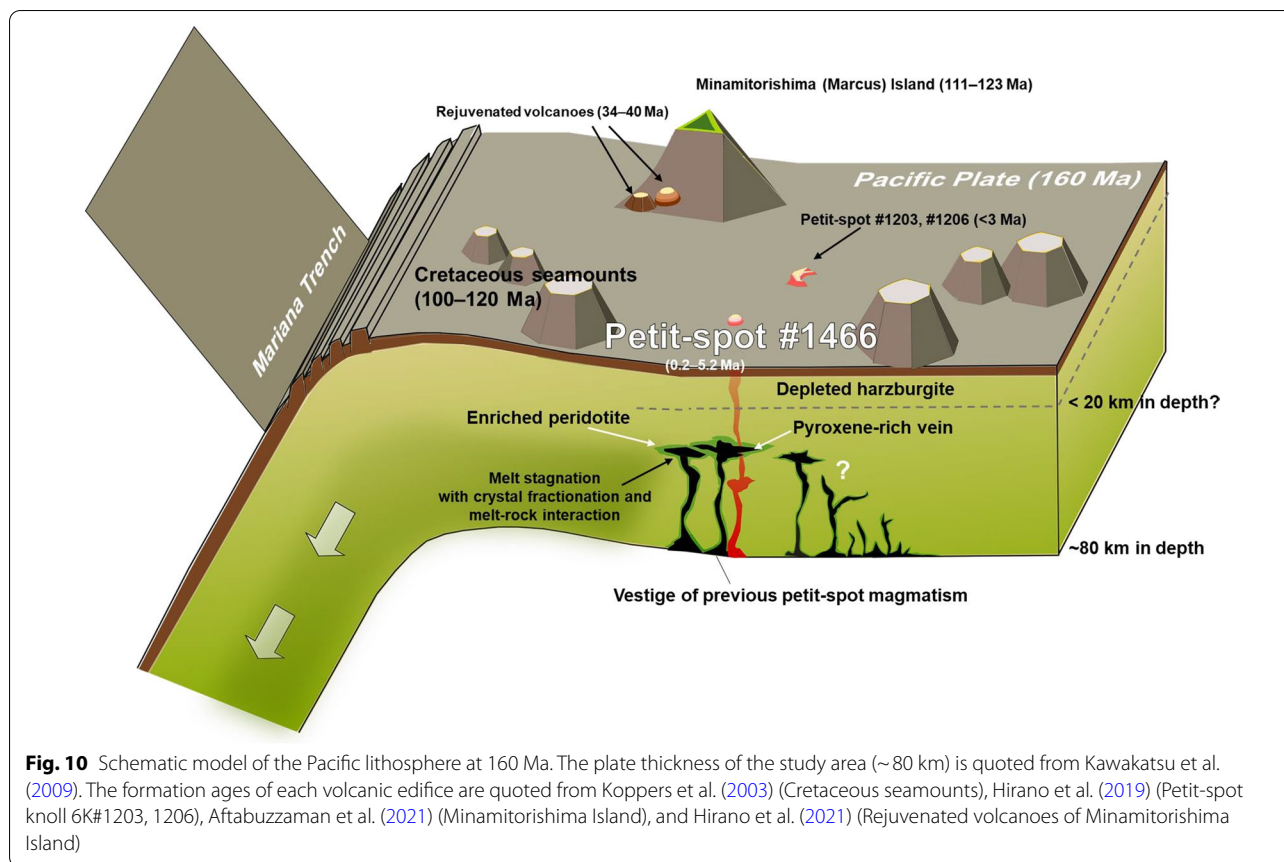
difference between the core and the spongy-textured part, including grain boundaries (where reacted with host magma; Fig. 6b–i) that support the occurrence of pre-entrapment fertilization. The comparatively recent magmatism at the lithosphere–asthenosphere boundary, generated by small amounts of volatiles and/or plate flexure (i.e., petit-spot), is the most probable metasomatic agent. As such, we argue that the metasomatic agent was petit-spot magma continuously percolated in the lithosphere prior to the host magma eruption. This inference is supported by the fact that the trace-element composition of the clinopyroxene in fertile xenoliths shows the same specific high field strength elements (i.e., HFSEs) anomaly as the petit-spot magma (Figs. 4b, 7a). Additionally, the MPSX-PR2 peridotite shows more pronounced anomalies of HFSEs than pyroxenites without notable Hf and Ti anomalies (Fig. 7a). This compositional relationship is similar to those between pyroxenite and enriched peridotite from Salt Lake Crater in Hawaii (Bizimis et al. 2003, 2005).

Pilet et al. (2016) suggested that the trace-element compositions of the clinopyroxene in peridotite xenoliths brought by the NW Pacific petit-spot volcano were exemplified by the metasomatic enrichment process of the petit-spot melt–depleted peridotite interaction. Those researchers also conducted a forward modeling exercise, which showed that the focused and porous melt from the lithosphere–asthenosphere boundary could form metasomatic veins in lithospheric mantle. The pyroxenites in the present study are good candidates for identification as metasomatic veins of the type just described. Yamamoto et al. (2009) provide the noble gas isotopic compositions of petit-spot peridotite xenoliths in NW Pacific petit-spots. The low $^4\text{He}/^{40}\text{Ar}^*$ (an asterisk indicates correction for atmospheric contribution) of peridotite xenoliths in the NW Pacific petit-spots indicates the injection of petit-spot magma into the lithospheric mantle prior to entrapment by the host magmatism (Yamamoto et al. 2009). Those researchers concluded that petit-spot volcanism should be recognized as a polygenetic magmatism with a long active period. Yamamoto et al. (2014) provided the residual pressure and two-pyroxene temperature recorded in peridotite xenoliths in NW Pacific petit-spot, and the obtained geothermal gradient is hotter than that of the GDH1 plate model and the half-space cooling model. Such a hot geotherm is interpreted as a localized feature restricted to the petit-spot region because widespread thermal anomalies are impossible to explain on the basis of present water depths and their associated isostatic adjustments (Turcotte and Schubert 2002; Yamamoto et al. 2014). In the western Pacific petit-spot region, the same phenomenon was observed.

6.3 The profile of Pacific lithosphere aged at 160 Ma

Combined with the barometric data by CO_2 fluid inclusions in pyroxene using Raman spectroscopy, we obtained a lithological structure of the oldest portion of the Pacific lithosphere. Although the two-pyroxene geobarometer of Mercier et al. (1984) and the geobarometer based on the pressure dependence of Ca partition between olivine and clinopyroxene (Köhler and Brey 1990) have been used so far, limitations of accuracy and precision mean they should be used with caution (Laurora et al. 2001; Yamamoto et al. 2014). For that reason, we used a form of geobarometry based on the density of CO_2 fluid inclusions, first proposed by Roedder (1965) and improved and updated by subsequent studies (Miller and Richter 1982; Roedder 1983; Rosso and Bodnar 1995; Seitz et al. 1996; Andersen and Neumann 2001; Yamamoto et al. 2002, 2007; Hagiwara et al. 2020, 2021). Since fluid inclusions in a mineral constituting a mantle xenolith should have existed in the mantle before being entrapped by magma, they can be used as a geobarometric probe for the host xenolith if the internal pressure of the fluid inclusions was in equilibrium with surrounding mantle. Even if the internal pressure of the fluid inclusion temporarily differed from that of its surroundings for some reason, this difference would be erased in a geochronologically short time (i.e., several days to years) in view of the physical properties (e.g., strain rate) of olivine and pyroxene (Yamamoto et al. 2008). The internal pressure of fluid inclusions in a xenolith may also respond to external pressure reduction during the transportation by magma. Under those conditions, olivine (having a low plastic deformation strength) may permit fluid inclusions within it to expand (e.g., Yamamoto et al. 2008). On the other hand, considering the plastic deformation strength of pyroxene or spinel and the eruption timescale of petit-spot magma (a few hundred days), the expansion of fluid inclusions during ascent and cooling may have a negligible in the original depth estimation (Sato et al. 2018; Yamamoto et al. 2011). All the same, the density (pressure) retained in CO_2 inclusions in natural samples does display variation and may have been affected by creep, decrepitation, or bursting during transport and cooling. In the face of such uncertainties, the measured values of inclusion density or pressure should be treated as limit indicators of minimum depth of formation, in the sense that the pressure and density of such an inclusion may diminish on ascent but should never increase.

The depth calculated by CO_2 inclusion of the MPSX-PR1 depleted harzburgite (>11.9 km) is the shallowest among the ultramafic xenoliths in this study, whereas that of the enriched peridotite (MPSX-PR2) is deeper, at 27.4 km (Fig. 8). Two pyroxenites (MPSX-PX1 and PX5) have equilibrium temperatures higher than depleted harzburgite (MPSX-PR1), representing residual depths of 18.5



km and 36.6 km, respectively, deeper than the depleted harzburgite. Additionally, upon applying the geothermobarometer of Putirka (2008) to estimate the origin of xenoliths, an increasing order of depth (from shallowest to deepest) was obtained as follows: the depleted peridotite (MPSX-PR1; 10.7 km), fertile peridotite (MPSX-PR2; 22.0 km), and pyroxenites with MPSX-PX5 (32.6 km); this order was consistent with that obtained from CO_2 inclusions (Fig. 8b). However, the MPSX-PX1 pyroxenite displayed a deeper value using Putirka's method (26.1 km) than that obtained for MPSX-PR2 peridotite, which differed from the depth-order obtained for these two rocks by the analysis of their CO_2 inclusions. It follows that the depth of MPSX-PX1 estimated using CO_2 inclusion should indeed be considered as a minimum depth only. Overall, these findings suggests that the origin of metasomatic pyroxene-rich veins and fertilized peridotite lies in a deeper part of the lithosphere than the depleted residual mantle (Fig. 8). Most of the petit-spot magma is expected to have stagnated at the stress-rotation field in the lithosphere, where the crystal fractionation and the melt-rock interaction occur, as was made

evident by the multiple-saturation experiment (Machida et al. 2017; Hirano and Machida 2022). The fertile components in this study, the pyroxenites in particular, could be derived from the mid-depth of the lithosphere assuming the about 80 km-thick lithosphere (i.e., ~40 km in depth; Kawakatsu et al. 2009) where petit-spot magma previously stagnated (Fig. 10). These pyroxenites, originating from metasomatic veins, consist with the so-called green core clinopyroxene xenocrysts as seen in the relicts of metasomatic veins in the Costa Rican petit-spot lavas (Buchs et al. 2013; Pilet et al. 2016).

As proposed by Yamamoto et al. (2014), petit-spot volcanoes erupted on the ocean floor should be considered to be just 'the tip of the iceberg,' and petit-spot melts could account for metasomatic veining in the lithosphere. As described above (Sect. 6.2), if the large thermal modification enough to change the overall geothermal structure of oceanic plate occurs, the water depth will become shallower (oceanic plate will float up), and then, this thermal modification would be a very local phenomenon. However, since it takes hundreds of thousands to millions of years to convert the geotherm, it would be difficult to find a magma reservoir sufficiently large to supply magma for such a long time. The partial melts on

the lithosphere–asthenosphere boundary (i.e., petit-spot magma) are therefore suggested to be the only underlying cause that can explain all phenomenon reported in this study. The oldest portion of the Pacific lithosphere has been modified, thermally and compositionally, by multiple petit-spot magmatisms prior to entrapment. In contrast, the depleted harzburgite sample, analogous to the pristine oceanic lithosphere, is a fundamental discovery that can yield insights into the chemistry of the deep oceanic lithosphere in its unaltered state. Although our data only allow us to see the local phenomena, such localized metasomatism in lithosphere could occur below the sea-floor without hotspots, and we have to reappraise the nature of subducting plate.

7 Conclusions

A petit-spot knoll was newly discovered on the abyssal plain south of the Minamitorishima (Marcus) Island. The silica-undersaturated petit-spot basalts erupted on the concave surface of the outer-rise swell because of subduction into the Mariana Trench. Ultramafic xenoliths of the oldest Pacific lithosphere could be divided into residual peridotite, fertile peridotite, and metasomatism-origin pyroxenites. Geochemistry and geothermobarometry of ultramafic xenoliths illustrated that metasomatic pyroxenite veins, formed via petit-spot magma–lithospheric peridotite interaction during the petit-spot magma stagnation, distribute in the oldest Pacific lithosphere. Moreover, we proved that depleted residual harzburgite practically exists in the uppermost portion of lithospheric mantle. The geotherm of the underlying lithosphere acquired from the equilibrium temperatures of xenoliths is much hotter than crustal age-appropriate temperature of oceanic lithosphere, which is probably caused by the relatively recent petit-spot magmatism. Although the following observation could not be verified from our samples, an identical phenomenon may occur not only in known petit-spot regions, but also in the plate-bending subduction fields in general, and/or where small amounts of volatiles are present.

Supplementary Information

The online version contains supplementary material available at <https://doi.org/10.1186/s40645-022-00518-y>.

Additional file 1: Figure S1. Entire BSE images of the ultramafic xenolith. These were taken using SEM–EDS, Hitachi S-3400, at Tohoku University. The dark shadows are hardware artifacts. The grain cores of ultramafic xenoliths are compositionally homogeneous. Analyzed points are indicated by circles and arrows. The colors of the symbols indicate mineral species (yellow-green is olivine, green is clinopyroxene, orange is orthopyroxene, and red is spinel). (a) MPSX-PR1 peridotite, (b) MPSX-PR2 peridotite, (c) MPSX-PX1 pyroxenite, (d) MPSX-PX2 pyroxenite, (e) MPSX-PX3 pyroxenite, (f) MPSX-PX4 pyroxenite, (g) MPSX-PX5 pyroxenite, and (h) MPSX-PX6 clinopyroxene xenocryst.

Additional file 2: Figure S2. Representative data and example of the Raman microscopic analysis for CO₂ fluid inclusion. (a) Raman spectrum of a CO₂ fluid inclusion in MPSX-PX5 pyroxenite. The peaks of volatile species except for CO₂ were lower than the detection limit of Raman spectroscopy. (b) An image of CO₂ fluid inclusions in the same sample.

Additional file 3. Supplementary information about the numerical process. The method of error calculation for the two pyroxene thermometry of Brey and Köhler (1990), the two pyroxene thermobarometry using the equation (36) and (38) of Putirka (2008), and the geobarometry of CO₂ inclusion in pyroxene by Raman spectroscopy are described. The process of depth-pressure conversion is also attached.

Additional file 4. Supplementary tables. **Table S1.** Major element compositions of olivine. **Table S2.** Major element compositions of clinopyroxene. **Table S3.** Major element compositions of orthopyroxene. **Table S4.** Major element compositions of spinel. **Table S5.** Trace element compositions of clinopyroxene. **Table S6.** Trace element compositions of orthopyroxene. **Table S7.** Data of Raman spectroscopy. **Table S8.** Average compositions of pyroxenes using the two pyroxene geothermobarometry.

Acknowledgements

We thank Captains E. Ukekura and T. Sakurai and the crews of the R/V Yokosuka and the submersible *SHINKAI 6500*, as well as the onboard scientific party during the YK16-01 cruise. I also owe my thanks to T. Tsujimori, R. Fukushima, S. Fukuhara, and Y. Matamura for their help and discussion on scientific matters. The authors would like to thank Enago (www.enago.jp) for the English-language review. This research was supported by the Cooperative Program (No. 110, 2021) of the Atmosphere and Ocean Research Institute at the University of Tokyo. We thank Prof. Bizimis and the anonymous reviewers for their thorough reviews, questions, and suggestions, which all helped us to improve the manuscript.

Author contributions

NH contributed to the interpretation of the data. NA cooperated to analyze using EPMA. JY and YH jointly analyzed the rock samples using micro-Raman spectroscopy. SM prepared the rock samples. AT and TM jointly undertook analysis using LA-ICP-MS. All authors read and approved the final manuscript.

Funding

This work was supported by the Japan Society for the Promotion of Science (Grant Numbers 18H01299, 18H03733, 20K04098).

Availability of data and materials

The datasets supporting the conclusions of this article are included within the article.

Declarations

Ethics approval and consent to participate

Not applicable.

Consent for publication

Not applicable.

Competing interests

The authors declare that they have no competing interests.

Author details

¹Graduate School of Science, Tohoku University, 6-3 Aramaki-Aoba, Aoba-Ku, Sendai 980-8578, Japan. ²Center for Northeast Asian Studies, Tohoku University, 41 Kawauchi, Aoba-Ku, Sendai 980-8576, Japan. ³Atmosphere and Ocean Research Institute, The University of Tokyo, 5-1-5, Kashiwanoha, Kashiwa 277-8564, Japan. ⁴Graduate School of Science, Kyushu University, Fukuoka 819-0395, Japan. ⁵Ocean Resources Research Center for Next Generation, Chiba Institution of Technology, 2-17-1 Tsudanuma, Narashino 275-0016, Japan. ⁶Earth Science Course, Kanazawa University, Kakuma, Kanazawa 920-1192, Japan. ⁷Graduate School of Science, Hokkaido University, Sapporo 060-0810, Japan. ⁸Research Institute for Marine Geodynamics, Japan Agency for Marine-Earth Science and Technology, Yokosuka 237-0061, Japan.

Received: 17 January 2022 Accepted: 22 October 2022
Published online: 12 November 2022

References

- Aftabuzzaman MR, Yomogoda K, Suzuki S, Takayanagi H, Ishigaki A, Machida S, Asahara Y, Yamamoto K, Hirano N, Sano S-I, Chiyonobu S, Bassi D, Iryu Y (2021) Multi-approach characterization of shallow-water carbonates off Minamitorishima and their depositional settings/history. *Island Arc* 30:e12400. <https://doi.org/10.1111/iar.12400>
- Andersen T, Neumann E-R (2001) Fluid inclusions in mantle xenoliths. *Lithos* 55:301–320. [https://doi.org/10.1016/S0024-4937\(00\)00049-9](https://doi.org/10.1016/S0024-4937(00)00049-9)
- Anma R, Armstrong R, Orihashi Y, Ike S-I, Shin K-C, Kon Y, Komiya T, Ota T, Kagashima S-I, Shibuya T, Yamamoto S, Veloso EE, Fanning M, Hervé F (2009) Are the Taitao granites formed due to subduction of the Chile ridge? *Lithos* 113:246–258. <https://doi.org/10.1016/j.lithos.2009.05.018>
- Akizawa N, Arai S (2009) Petrologic profile of peridotite layers under a possible Moho in the northern Oman ophiolite: an example from Wadi Fizh. *J Mineral Petrol Sci* 104:389–394. <https://doi.org/10.2465/jmps.090622a>
- Akizawa N, Arai S, Tamura A (2012) Behavior of MORB magmas at uppermost mantle beneath a fast-spreading axis: an example from Wadi Fizh of the northern Oman ophiolite. *Contrib Mineral Petrol* 164:601–625. <https://doi.org/10.1007/s00410-012-0762-4>
- Akizawa N, Miyake A, Ishikawa A, Tamura A, Terada Y, Uesugi K, Takeuchi A, Arai S, Tanaka C, Igami Y, Suzuki K, Kogiso T (2017) Metasomatic PGE mobilization by carbonatitic melt in the mantle: evidence from sub- μ m-scale sulfide–carbonaceous glass inclusion in Tahitian harzburgite xenolith. *Chem Geol* 475:87–104. <https://doi.org/10.1016/j.chemgeo.2017.10.037>
- Akizawa N, Ohara Y, Okino K, Ishizuka O, Yamashita H, Machida S, Sanfilippo A, Basch V, Snow JE, Sen A, Hirauchi K, Michibayashi K, Harigane Y, Fujii M, Asanuma H, Hirata T (2021) Geochemical characteristics of back-arc basin lower crust and upper mantle at final spreading stage of Shikoku Basin: an example of Mado Megamullion. *Prog Earth Planet Sci* 8:1–24. <https://doi.org/10.1186/s40645-021-00454-3>
- Arai S, Matsukage K (1996) Petrology of the gabbro-troctolite-peridotite complex from Hess Deep, equatorial Pacific: implications for mantle-melt interaction within the oceanic lithosphere. *Proc ODP Sci Res* 147:135–155. <https://doi.org/10.2973/odp.proc.sr.147.008.1996>
- Ashley AW, Bizimis M, Peslier AH, Jackson M, Konter JG (2020) Metasomatism and hydration of oceanic lithosphere: a case study of peridotite xenoliths from Samoa. *J Petrol* 61:egaa028. <https://doi.org/10.1093/ptrology/egaa028>
- Bizimis M, Sen G, Salters VJM (2003) Hf–Nd isotope decoupling in the oceanic lithosphere: constraints from spinel peridotites from Oahu, Hawaii. *Earth Planet Sci Lett* 207:43–58. [https://doi.org/10.1016/S0012-821X\(03\)00598-3](https://doi.org/10.1016/S0012-821X(03)00598-3)
- Bizimis M, Sen G, Salters VJM, Keshav S (2005) Hf–Nd–Sr isotope systematics of garnet pyroxenites from Salt Lake Crater, Oahu, Hawaii: evidence for a depleted component in Hawaiian volcanism. *Geochim Cosmochim Acta* 69:2629–2646. <https://doi.org/10.1016/j.gca.2005.01.005>
- Bizimis M, Griselin M, Lassiter JC, Salters VJM, Sen G (2007) Ancient recycled mantle lithosphere in the Hawaiian plume: osmium–hafnium isotopic evidence from peridotite mantle xenoliths. *Earth Planet Sci Lett* 257:259–273. <https://doi.org/10.1016/j.epsl.2007.02.036>
- Bizimis M, Salters VJM, Garcia MO, Norman MD (2013) The composition and distribution of the rejuvenated component across the Hawaiian plume: Hf–Nd–Sr–Pb isotope systematics of Kaula lavas and pyroxenite xenoliths. *Geochem Geophys Geosyst* 14:4458–4478. <https://doi.org/10.1002/ggge.20250>
- Blackman DK, Canales JP, Harding A (2009) Geophysical signatures of oceanic core complexes. *Geophys J Int* 178:593–613. <https://doi.org/10.1111/j.1365-246X.2009.04184.x>
- Boschman LM, van Hinsbergen DJJ (2016) On the enigmatic birth of the Pacific Plate within the Panthalassa Ocean. *Sci Adv* 2:e1600022. <https://doi.org/10.1126/sciadv.1600022>
- Brey GP, Köhler T (1990) Geothermobarometry in four-phase Lherzolites II, new thermobarometers, and practical assessment of existing their barometers. *J Petrol* 31:1353–1378. <https://doi.org/10.1016/j.jcrte.2007.10.012>
- Buchs DM, Pilet S, Cosca M, Flores KE, Bandini AN, Baumgartner PO (2013) Low-volume intraplate volcanism in the Early/Middle Jurassic Pacific basin documented by accreted sequences in Costa Rica. *Geochem Geophys Geosyst* 14:1552–1568. <https://doi.org/10.1002/ggge.20084>
- Burnard PG, Farley KA, Turner G (1998) Multiple fluid pulses in a Samoan harzburgite. *Chem Geol* 147:99–114. [https://doi.org/10.1016/S0009-2541\(97\)00175-7](https://doi.org/10.1016/S0009-2541(97)00175-7)
- Byerly BL, Jackson MG, Bizimis M (2021) Carbonatite versus silicate melt metasomatism impacts grain scale $^{87}\text{Sr}/^{86}\text{Sr}$ and $^{143}\text{Nd}/^{144}\text{Nd}$ heterogeneity in polynesian mantle peridotite xenoliths. *Geochem Geophys Geosyst* 22:e2021GC009749. <https://doi.org/10.1029/2021GC009749>
- Carlson RL, Snow LR, Wilkens RH (1988) Density of old oceanic crust: an estimate derived from downhole logging on ODP leg 102. *Proc Ocean Drill Sci Results* 102:63–68. <https://doi.org/10.2973/odp.proc.sr.102.124.1988>
- Clague DA, Frey FA (1982) Petrology and trace element geochemistry of the Honolulu Volcanics, Oahu: implications for the oceanic mantle below Hawaii. *J Petrol* 23:447–504. <https://doi.org/10.1093/ptrology/23.3.447>
- Clague DA (1988) Petrology of ultramafic xenoliths from Loihi Seamount, Hawaii. *J Petrol* 29:1161–1186. <https://doi.org/10.1093/ptrology/29.6.1161>
- Coltorti M, Bonadiman C, Hinton RW, Siena F, Upton BGG (1999) Carbonatite metasomatism of the oceanic upper mantle: evidence from clinopyroxenes and glasses in ultramafic xenoliths of Grande Comore, Indian Ocean. *J Petrol* 40:133–165. <https://doi.org/10.1093/ptrology/40.1.133>
- Dawson JB (1984) Contrasting types of upper-mantle metasomatism? *Dev Petrol* 11:289–294. <https://doi.org/10.1016/B978-0-444-42274-3.50030-5>
- Dick HJB, Natland J (1996) Late-stage melt evolution and transport in the shallow mantle beneath the East Pacific Rise. *Proc ODP Sci Results* 147:103–134. <https://doi.org/10.2973/odp.proc.sr.147.007.1996>
- Dieu JJ (1995) Mineral compositions in Leg 144 lavas and ultramafic xenoliths: the roles of cumulates and carbonatite metasomatism in magma petrogenesis. *Proc Ocean Drill Progr Sci Res*. <https://doi.org/10.2973/odp.proc.sr.144.029.1995>
- Dilek Y, Morishita T (2009) Melt migration and uppermantle evolution during incipient arc construction: Jurassic eastern Mirdita ophiolite, Albania. *Island Arc* 18:551–554. <https://doi.org/10.1111/j.1440-1738.2009.00692.x>
- Dilek Y, Furnes H (2014) Ophiolites and their origins. *Elements* 10:93–100. <https://doi.org/10.2113/gselements.10.2.93>
- Escartín J, Smith D, Cann J, Schouten H, Langmuir CH, Escrig S (2008) Central role of detachment faults in accretion of slow-spreading oceanic lithosphere. *Nature* 455:90–94. <https://doi.org/10.1038/nature07333>
- Fodor RV, Bauer GR, Keil K (1982) Ultramafic inclusions and megacrysts in olivine nephelinite, Aitutaki Island, Cook Islands. *N Z J Geol Geophys* 25:67–76. <https://doi.org/10.1080/00288306.1982.10422505>
- Goodenough KM, Thomas RJ, Styles MT, Schofield DI, MacLeod CJ (2014) Records of ocean growth and destruction in the Oman–UAE ophiolite. *Elements* 10:109–114. <https://doi.org/10.2113/gselements.10.2.109>
- Gripp AE, Gordon RG (1990) Current plate velocities relative to the hotspots incorporating the NUVEL-1 global plate motion model. *Geophys Res Lett* 17:1109–1112. <https://doi.org/10.1029/GL0171008p01109>
- Hagiwara Y, Torimoto J, Yamamoto J (2020) Pressure measurement and detection of small H₂O amounts in high-pressure H₂O–CO₂ fluid up to 141 MPa using Fermi diad splits and bandwidths of CO₂. *J Raman Spectrosc*. <https://doi.org/10.1002/jrs.5865>
- Hagiwara Y, Yoshida K, Yoneda A, Torimoto J, Yamamoto J (2021) Experimental variable effects on laser heating of inclusions during Raman spectroscopic analysis. *Chem Geol* 559:119928. <https://doi.org/10.1016/j.chemgeo.2020.119928>
- Harigane Y, Mizukami T, Morishita T, Michibayashi K, Abe N, Hirano N (2011) Direct evidence for upper mantle structure in the NW Pacific Plate: microstructural analysis of a petit-spot peridotite xenolith. *Earth Planet Sci Lett* 302:194–202. <https://doi.org/10.1016/j.epsl.2010.12.011>
- Harigane Y, Michibayashi K, Morishita T, Tamura A, Hashimoto S, Snow JE (2022) Deformation beneath Gakkell Ridge, Arctic Ocean: from mantle flow to mantle shear in a sparsely magmatic spreading zone. *Tectonophysics* 822:229186. <https://doi.org/10.1016/j.tecto.2021.229186>
- Hauri EH, Shimizu N, Dieu JJ, Hart SR (1993) Evidence for hotspot-related carbonatite metasomatism in the oceanic upper mantle. *Nature* 365:221–227. <https://doi.org/10.1038/365221a0>
- Hauri EH, Hart SR (1994) Constraints on melt migration from mantle plume: a trace element study of peridotite xenoliths from Savai'i Western Samoa.

- J Geophys Res 99(B12):24301–24321. <https://doi.org/10.1029/94JB01553>
- Hein JR, Koschinsky A, Bau M, Manheim FT, Kang JK, Roberts L (1999) Cobalt-rich ferromanganese crusts in the Pacific. In: Cronan DS (ed) Handbook of marine mineral deposits. CRC Press, Boca Raton, pp 239–279
- Hirano N, Yamamoto J, Kagi H, Ishii T (2004) Young, olivine xenocryst-bearing alkali-basalt from the oceanward slope of the Japan Trench. *Contrib Mineral Petrol* 148:47–54. <https://doi.org/10.1007/s00410-004-0593-z>
- Hirano N, Takahashi E, Yamamoto J, Abe N, Ingle SP, Kaneoka I, Hirata T, Kimura J-I, Hirata T, Ishii T, Ogawa Y, Machida S, Suyehiro K (2006) Volcanism in response to plate flexure. *Science* 313:1426–1428. <https://doi.org/10.1126/science.1128235>
- Hirano N, Koppers AAP, Takahashi A, Fujiwara T, Nakanishi M (2008) Seamounts, knolls and petit spot monogenetic volcanoes on the subducting Pacific plate. *Basin Res* 20:543–553. <https://doi.org/10.1111/j.1365-2117.2008.00363.x>
- Hirano N (2011) Petit-spot volcanism: a new type of volcanic zone discovered near a trench. *Geochem J* 45:157–167. <https://doi.org/10.2343/geochemj.1.0111>
- Hirano N, Machida S, Sumino H, Shimizu K, Tamura A, Morishita T, Iwano H, Sakata S, Ishii T, Arai S, Yoneda S, Danhara T, Hirata T (2019) Petit-spot volcanoes on the oldest portion of the Pacific Plate. *Deep Sea Res Part I* 154:103142. <https://doi.org/10.1016/j.dsr.2019.103142>
- Hirano N, Sumino H, Morishita T, Machida S, Kawano T, Yasukawa K, Hirata T, Kato Y, Ishii T (2021) A Paleogene magmatic overprint on Cretaceous seamounts of the western Pacific. *Island Arc* 30:e12386. <https://doi.org/10.1111/iar.12386>
- Hirano N, Machida S (2022) The mantle structure below petit-spot volcanoes. *Commun Earth Environ* 3:110. <https://doi.org/10.1038/s43247-022-00438-1>
- Jackson ED, Wright TL (1970) Xenoliths in the Honolulu Volcanic Series, Hawaii. *J Petrol* 11:405–433. <https://doi.org/10.1093/ptrology/11.2.405>
- Jackson MG, Shirey SB, Hauri EH, Kurz MD, Rizo H (2016) Peridotite xenoliths from the Polynesian Austral and Samoa hotspots: implications for the destruction of ancient 187Os and 142Nd isotopic domains and the preservation of Hadean 129Xe in the modern convecting mantle. *Geochim Cosmochim Acta* 185:21–43. <https://doi.org/10.1016/j.gca.2016.02.011>
- Jochum KP, Nohl U (2008) Reference materials in geochemistry and environmental research and the GeoReM database. *Chem Geol* 253:50–53. <https://doi.org/10.1016/j.chemgeo.2008.04.002>
- Kaneda K, Kodaira S, Nishizawa A, Morishita T, Takahashi N (2010) Structural evolution of preexisting oceanic crust through intraplate igneous activities in the Marcus-Wake seamount chain. *Geochem Geophys Geosyst* 11:Q10014. <https://doi.org/10.1029/2010GC003231>
- Kawakami Y, Yamamoto J, Kagi H (2003) Micro-Raman densimeter for CO₂ inclusions in mantle-derived minerals. *Appl Spectrosc* 57:1333–1339. <https://doi.org/10.1366/00037020322554473>
- Kawakatsu H, Kumar P, Takei Y, Shinohara M, Kanazawa T, Araki E, Suyehiro K (2009) Seismic evidence for sharp lithosphere-asthenosphere boundaries of oceanic plates. *Science* 324:499–502. <https://doi.org/10.1126/science.1169499>
- Köhler T, Brey GP (1990) Calcium exchange between olivine and clinopyroxene calibrated as a geothermobarometer for natural peridotites from 2 to 60 kb with applications. *Geochim Cosmochim Acta* 54:2375–2388. [https://doi.org/10.1016/0016-7037\(90\)90226-B](https://doi.org/10.1016/0016-7037(90)90226-B)
- Koppers AAP, Staudigel H, Pringle MS, Wijbrans JR (2003) Short-lived and discontinuous intra-plate volcanism in the South Pacific: hotspots or extensional volcanism? *Geochem Geophys Geosyst* 4:1089. <https://doi.org/10.1029/2003GC000533>
- Langmuir CH, Klein EM, Plank T (1992) Petrological systematics of mid-ocean ridge basalts: constraints on melt generation beneath ocean ridges. In: Morgan JP, Blackman DK, Sinton JM (eds) Mantle flow and melt generation at mid ocean ridges. AGU, Washington, DC, pp 183–280. <https://doi.org/10.1029/GM071p0183>
- Laukert G, Handt AVD, Hellebrand E, Snow JE, Hoppe P, Klügel A (2014) High-pressure reactive melt stagnation recorded in abyssal pyroxenites from the ultraslow-spreading Lena Trough, Arctic Ocean. *J Petrol* 55:427–458. <https://doi.org/10.1093/ptrology/egt073>
- Laurora A, Mazzucchelli M, Rivalenti G, Vannucci R, Zanetti A, Barbieri MA, Cingolani CA (2001) Metasomatism and melting in carbonated peridotite xenoliths from the mantle wedge: the Gobernador Gregores Case (Southern Patagonia). *J Petrol* 42:69–87. <https://doi.org/10.1093/ptrology/42.1.69>
- Liang Z, Xiao Y, Thakurta J, Su B, Chen C, Bai Y, Sakyi PA (2018) Exsolution lamellae in olivine grains of dunite units from different types of Mafic-Ultramafic complexes. *Acta Geol Sin (english Edition)* 92:586–599. <https://doi.org/10.1111/1755-6724.13544>
- Longerich HP, Jackson SE, Gunther D (1996) Laser ablation inductively coupled plasma mass spectrometric transient signal data acquisition and analyte concentration calculation. *J Anal at Spectrom* 11:899–904. <https://doi.org/10.1039/ja9961100899>
- Machida S, Hirano N, Sumino H, Hirata T, Yoneda S, Kato Y (2015) Petit-spot geology reveals melts in upper-most asthenosphere dragged by lithosphere. *Earth Planet Sci Lett* 426:267–279. <https://doi.org/10.1016/j.epsl.2015.06.018>
- Machida S, Kogiso T, Hirano N (2017) Petit-spot as definitive evidence for partial melting in the asthenosphere caused by CO₂. *Nat Commun* 8:14302. <https://doi.org/10.1038/ncomms14302>
- Machida S, Sato T, Yasukawa K, Nakamura K, Iijima K, Nozaki T, Kato Y (2021) Visualisation method for the broad distribution of seafloor ferromanganese deposits. *Mar Georesour Geotechnol* 39:267–279. <https://doi.org/10.1080/1064119X.2019.1696432>
- Mallick S, Standish JJ, Bizimis M (2015) Constraints on the mantle mineralogy of an ultra-slow ridge: hafnium isotopes in abyssal peridotites and basalts from the 9–25°E Southwest Indian Ridge. *Earth Planet Sci Lett* 410:42–53. <https://doi.org/10.1016/j.epsl.2014.10.048>
- Meckel TA, Coffin MF, Mosher S, Symonds P, Bernardel G, Mann P (2003) Underthrusting at the Hjort Trench, Australian-Pacific plate boundary: incipient subduction? *Geochem Geophys Geosyst* 4:1099. <https://doi.org/10.1029/2002GC000498>
- Mercier J-C, Benoit V, Girardeau J (1984) Equilibrium state of diopside-bearing harzburgites from ophiolites: geobarometric and geodynamic implications. *Contrib Mineral Petrol* 85:391–403. <https://doi.org/10.1007/BF01150295>
- Miller C, Richter W (1982) Solid and fluid phases in lherzolite and pyroxenite inclusions from the Hoggar central Sahara. *Geochem J* 16:263–277. <https://doi.org/10.2343/geochemj.16.263>
- Moore JG, Fornari DJ, Clague DA (1985) Basalts from the 1877 submarine eruption of Mauna Loa, Hawaii; new data on the variation of palagonitization rate with temperature. *U S Geol Surv Bull* 1663:1–11. <https://doi.org/10.3133/b1663>
- Morimoto N (1988) Nomenclature of pyroxenes. *Mineral Petrol* 39:55–76. <https://doi.org/10.1007/BF01226262>
- Müller RD, Sdrolias M, Gaina C, Roest WR (2008) Age, spreading rates, and spreading asymmetry of the world's ocean crust. *Geochem Geophys Geosyst* 9:Q04006. <https://doi.org/10.1029/2007GC001743>
- Niu Y, Langmuir CH, Kinzler RJ (1997) The origin of abyssal peridotites: a new perspective. *Earth Planet Sci Lett* 152:251–265. [https://doi.org/10.1016/S0012-821X\(97\)00119-2](https://doi.org/10.1016/S0012-821X(97)00119-2)
- Nayar KG, Sharqawy MH, Banchik LD, Lienhard JH (2016) Thermophysical properties of seawater: a review and new correlations that include pressure dependence. *Desalination* 390:1–24. <https://doi.org/10.1016/j.desal.2016.02.024>
- Odake S, Fukura S, Kagi H (2008) High precision in Raman frequency achieved using real-time calibration with a neon emission line: application to three-dimensional stress mapping observations. *Appl Spectrosc* 62:1084–1087. <https://doi.org/10.1366/000370208786049169>
- Ohara Y, Yoshida T, Kato Y, Kasuga S (2001) Giant Megamullion in the Parece Vela Backarc Basin. *Mar Geophys Res* 22:47–61. <https://doi.org/10.1023/A:1004818225642>
- Olive JA, Behn M, Turcholke B (2010) The structure of oceanic core complexes controlled by the depth distribution of magma emplacement. *Nat Geosci* 3:491–495. <https://doi.org/10.1038/ngeo888>
- Pearce NJG, Perkins WT, Westgate JA, Gorton MP, Jackson SE, Neal CR, Chenerly SP (1997) A compilation of new and published major and trace element data for NIST SRM 610 and NIST SRM 612 glass reference materials. *Geostand Newsl* 21:115–144. <https://doi.org/10.1111/j.1751-908X.1997.tb00538.x>
- Pilet S, Abe N, Rochat L, Kaczmarek M-A, Hirano N, Machida S, Buchs DM, Baumgarther PO, Müntener O (2016) Pre-subduction metasomatic

- enrichment of the oceanic lithosphere induced by plate flexure. *Nat Geosci* 9:898–903. <https://doi.org/10.1038/ngeo2825>
- Pitzer KS, Sterner SM (1995) Equations of state valid continuously from zero to extreme pressures with H₂O and CO₂ as examples. *Int J Thermophys* 16:511–518. <https://doi.org/10.1007/BF01441917>
- Plank T, Langmuir CH (1992) Effects of melting regime on the composition of the oceanic crust. *J Geophys Res* 97(B13):19749–19770. <https://doi.org/10.1029/92JB01769>
- Pressling N, Morris A, John BE, MacLeod CJ (2012) The internal structure of an oceanic core complex: an integrated analysis of oriented borehole imagery from IODP Hole U1309D (Atlantis Massif). *Geochem Geophys Geosyst* 13:Q04G10. <https://doi.org/10.1029/2012GC004061>
- Putirka KD (2008) Thermometers and barometers for volcanic systems. *Rev Mineral Geochem* 69:61–120. <https://doi.org/10.2138/rmg.2008.69.3>
- Qi Q, Beard BL, Jin T, Taylor LA (1994) Petrology and geochemistry of Al-augite and Cr-diopside Group Mantle Xenoliths from Tahiti, Society Islands. *Int Geol Rev* 36:152–178. <https://doi.org/10.1080/00206819409465453>
- Regelous M, Weinzierl CG, Haase KM (2016) Controls on melting at spreading ridges from correlated abyssal peridotite–mid-ocean ridge basalt compositions. *Earth Planet Sci Lett* 449:1–11. <https://doi.org/10.1016/j.epsl.2016.05.017>
- Roedder E (1965) Liquid CO₂ inclusions in olivine bearing nodules and phenocrysts from basalts. *Am Miner* 50:1746–1782
- Roedder E (1983) Geobarometry of ultramafic xenoliths from Loihi Seamount, Hawaii, on the basis of CO₂ inclusions in olivine. *Earth Planet Sci Lett* 66:369–379
- Rochat L, Pilet S, Müntener O, Duret T, Baumgartner L, Abe N, Hirano N (2017) Garnet xenocryst from petit-spot lavas as an indicator for off-axis mantle refertilization at intermediate spreading ridges. *Geology* 45:1091–1094. <https://doi.org/10.1130/G39427.1>
- Rosso KM, Bodnar RJ (1995) Microthermometric and Raman spectroscopic detection limits of CO₂ in fluid inclusions and the Raman spectroscopic characterization of CO₂. *Geochim Cosmochim Acta* 59:3961–3975. [https://doi.org/10.1016/0016-7037\(95\)94441-H](https://doi.org/10.1016/0016-7037(95)94441-H)
- Sato Y, Hirano N, Machida S, Yamamoto J, Nakanishi M, Ishii T, Taki A, Yasukawa K, Kato Y (2018) Direct ascent to the surface of asthenospheric magma in a region of convex lithospheric flexure. *Int Geol Rev* 60:1231–1243. <https://doi.org/10.1080/00206814.2017.1379912>
- Seitz JC, Pasteris JD, Chou I-M (1996) Raman spectroscopic characterization of gas mixtures. II. Quantitative composition and pressure determination of the CO₂–CH₄ system. *Am J Sci* 296:577–600. <https://doi.org/10.2475/ajs.296.6.577>
- Sen G, Frey FA, Shimizu N, Leeman WP (1993) Evolution of the lithosphere beneath Oahu, Hawaii: rare earth element abundances in mantle xenoliths. *Earth Planet Sci Lett* 119:53–69. [https://doi.org/10.1016/0012-821X\(93\)90006-U](https://doi.org/10.1016/0012-821X(93)90006-U)
- Sen G, Keshav S, Bizimis M (2005) Hawaiian xenoliths and magmas: Composition and thermal character of the lithosphere. *Am Mineral* 90:871–887. <https://doi.org/10.2138/am.2005.1731>
- Sen A, Snow JE, Ohara Y, Hirauchi K, Kouketsu Y, Sanfilippo A, Basch V, Harigane Y, Fujii M, Okino K, Akizawa N (2021) Melting and evolution of amphibole-rich back-arc abyssal peridotites at the Mado Megamullion, Shikoku Basin. *Geochem Geophys Geosyst* 22:e2021GC010013. <https://doi.org/10.1029/2021GC010013>
- Seyler M, Toplis MJ, Lorand JO, Luguét A, Cannat M (2001) Clinopyroxene microtextures reveal incompletely extracted melts in abyssal peridotites. *Geology* 29:155–158. [https://doi.org/10.1130/0091-7613\(2001\)029%3C0155:CMRIEM%3E2.0.CO;2](https://doi.org/10.1130/0091-7613(2001)029%3C0155:CMRIEM%3E2.0.CO;2)
- Shaw CSJ, Heidelbach F, Dingwell DB (2006) The origin of reaction textures in mantle peridotite xenoliths from Sal Island, Cape Verde: the case for “metasomatism” by the host lava. *Contrib Mineral Petrol* 151:681–697. <https://doi.org/10.1007/s00410-006-0087-2>
- Snortum E, Day JMD, Jackson MG (2019) Pacific lithosphere evolution inferred from Aitutaki mantle xenoliths. *J Petrol* 60:1753–1772. <https://doi.org/10.1093/ptrology/egz047>
- Su B-X, Zhang H-F, Sakyi PA, Yang Y-H, Ying J-F, Tang Y-J, Qin K-Z, Xiao Y, Zhao X-M, Mao Q, Ma Y-G (2011) The origin of spongy texture in minerals of mantle xenoliths from the Western Qinling, central China. *Contrib Mineral Petrol* 161:465–482. <https://doi.org/10.1007/s00410-010-0543-x>
- Stein CA, Stein S (1992) A model for the global variation in oceanic depth and heat flow with lithospheric age. *Nature* 359:123–129. <https://doi.org/10.1038/359123a0>
- Sun S-S, McDonough WF (1989) Chemical and isotopic systematics of oceanic basalts: implications for mantle composition and processes. *Geol Soc Spec Publ* 42:313–345. <https://doi.org/10.1144/GSL.SP.1989.042.01.19>
- Takahashi E, Uto K, Schilling J-G (1987) Primary magma compositions and Mg/Fe ratios of their mantle residues along Mid Atlantic Ridge 29° N to 73° N. Technical report of ISEI Okayama University Series A 9:1–4
- Tivey MA, Sager WW, Lee S-M, Tominaga M (2006) Origin of the Pacific Jurassic quiet zone. *Geology* 34:789–792. <https://doi.org/10.1130/G22894.1>
- Toh S, Shimobayashi N (2000) Microtextures in Ca–Mg–Fe pyroxenes. *Jpn Mag Mineral Petrol Sci* 29:35–44. <https://doi.org/10.2465/gkk.29.35>
- Tracy RJ (1980) Petrology and genetic significance of an ultramafic xenolith suite from Tahiti. *Earth Planet Sci Lett* 48:80–96. [https://doi.org/10.1016/0012-821X\(80\)90172-7](https://doi.org/10.1016/0012-821X(80)90172-7)
- Turcotte DL, Schubert G (2002) *Geodynamics*, 2nd edn. Cambridge University Press, Cambridge, p 472. <https://doi.org/10.1002/gj.987>
- Wagner TP, Grove TL (1998) Melt/harzburgite reaction in the petrogenesis of tholeiitic magma from Kilauea volcano, Hawaii. *Contrib Mineral Petrol* 131:1–12. <https://doi.org/10.1007/s004100050374>
- Warren JM (2016) Global variations in abyssal peridotite compositions. *Lithos* 248–251:193–219. <https://doi.org/10.1016/j.lithos.2015.12.023>
- Wass SY (1979) Multiple origins of clinopyroxenes in alkali basaltic rocks. *Lithos* 12:115–132. [https://doi.org/10.1016/0024-4937\(79\)90043-4](https://doi.org/10.1016/0024-4937(79)90043-4)
- Weller OM, Copley A, Miller WGR, Palin RM, Dyck B (2019) The relationship between mantle potential temperature and oceanic lithosphere buoyancy. *Earth Planet Sci Lett* 518:86–99. <https://doi.org/10.1016/j.epsl.2019.05.005>
- Wilshire HG, Shervais JW (1975) Al-augite and Cr-diopside ultramafic xenoliths in basaltic rocks from western United States. *Phys Chem Earth* 9:257–272. [https://doi.org/10.1016/0079-1946\(75\)90021-X](https://doi.org/10.1016/0079-1946(75)90021-X)
- Yamamoto J, Kagi H, Kaneoka I, Lai Y, Prikhod'ko VS, Arai S (2002) Fossil pressures of fluid inclusions in mantle xenoliths exhibiting rheology of mantle minerals: implications for the geobarometry of mantle minerals using micro Raman spectroscopy. *Earth Planet Sci Lett* 198:511–519. [https://doi.org/10.1016/S0012-821X\(02\)00528-9](https://doi.org/10.1016/S0012-821X(02)00528-9)
- Yamamoto J, Kagi H, Kawakami Y, Hirano N, Nakamura M (2007) Paleo-Moho depth determined from the pressure of CO₂ fluid inclusions: Raman spectroscopic barometry of mantle- and crust-derived rocks. *Earth Planet Sci Lett* 253:369–377. <https://doi.org/10.1016/j.epsl.2006.10.038>
- Yamamoto J, Kagi H (2008) Application of micro-Raman densimeter for CO₂ fluid inclusions: a probe for elastic strengths of mantle minerals. *Eur J Mineral* 20:529–535. <https://doi.org/10.1127/0935-1221/2008/0020-1825>
- Yamamoto J, Hirano N, Abe N, Hanyu T (2009) Noble gas isotopic compositions of mantle xenoliths from northwestern Pacific lithosphere. *Chem Geol* 268:313–323. <https://doi.org/10.1016/j.chemgeo.2009.09.009>
- Yamamoto J, Otsuka K, Ohfuji H, Ishibashi H, Hirano N, Kagi H (2011) Retentivity of CO₂ in fluid inclusions in mantle minerals. *Eur J Mineral* 23:805–815. <https://doi.org/10.1127/0935-1221/2011/0023-2150>
- Yamamoto J, Korenaga J, Hirano N, Kagi H (2014) Melt-rich lithosphere–asthenosphere boundary inferred from petit-spot volcanoes. *Geology* 42:967–970. <https://doi.org/10.1130/G35944.1>
- Yamamoto J, Ishibashi H, Nishimura K (2017) Cooling rate responsiveness of pyroxene geothermometry. *Geochem J* 51:457–467. <https://doi.org/10.2343/geochemj.2.0477>
- Yamamoto J, Kawano T, Takahata N, Sano Y (2018) Noble gas and carbon isotopic compositions of petit-spot lavas from southeast of Marcus Island. *Earth Planet Sci Lett* 497:139–148. <https://doi.org/10.1016/j.epsl.2018.06.020>
- Zong K, Liu Y (2018) Carbonatite metasomatism in the lithospheric mantle: implications for cratonic destruction in North China. *Sci China Earth Sci* 61:711–729. <https://doi.org/10.1007/s11430-017-9185-2>

Publisher's Note

Springer Nature remains neutral with regard to jurisdictional claims in published maps and institutional affiliations.